3.4.3 Distribution D2 (radially decreasing thickness)

The experimental results of the third axisymmetric case, a circular membrane with radially decreasing thickness, are presented here. A linear decrease in the membrane's thickness towards the edge is considered here. The membrane was fabricated using a conical mold that has a positive slope of about 4.8°, which results in a thickness difference of 6.35 mm (0.25 in) between the center and edge of the membrane. Figure 3.22A shows the thickness distribution of the axisymmetric membrane of this case. The initial thicknesses of the membrane were measured to be 1.92 mm (0.076 in) at the edge and 8.27 mm (0.326 in) at the center, giving $\eta = 0.232$. (The volume of rubber material here is about 1.5× that of the uniform thickness membrane.) Figures 3.22B–3.22E show snapshots of the membrane at four instants of time during inflation.

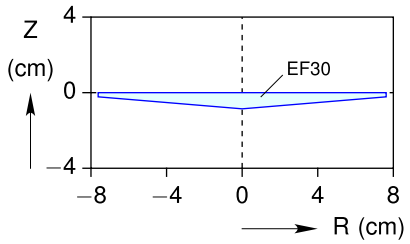

A. Membrane cross-section

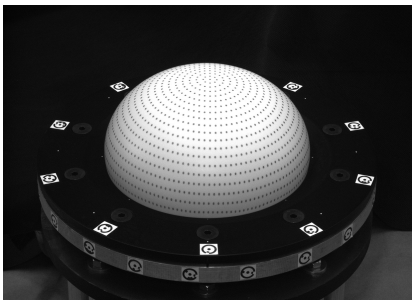

B. $t = 300$ s

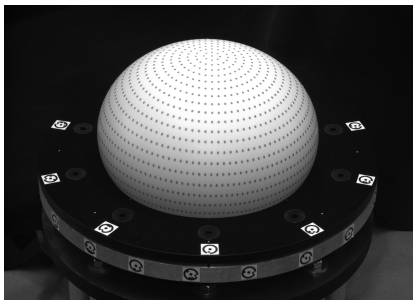

C. $t = 450$ s

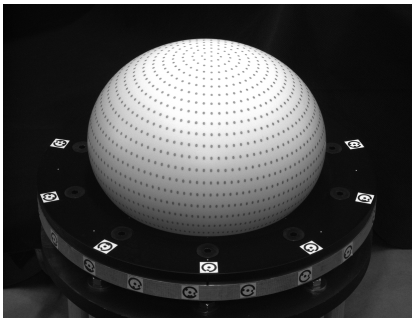

D. $t = 600$ s

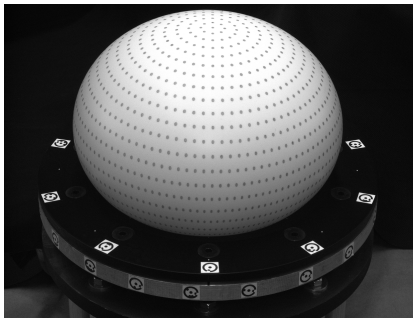

E. $t = 897.5$ s

Figure 3.22: Photographs of the nonuniform thickness membrane (distribution D2) at selected times during inflation.

The pressure and volume-change histories during inflation are demonstrated in Figures 3.23A and 3.23B. The pressure-volume cross plot is shown in Figure 3.23C which shows an 'S-shape' behavior in response similar to the previous axisymmetric membranes.

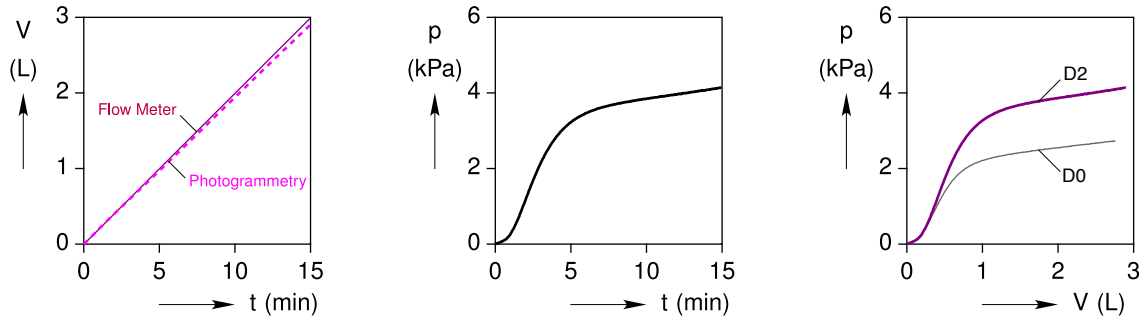

A. Volume history B. Pressure history C. Pressure-volume

Figure 3.23: Structural response of the nonuniform membrane (distribution D2).

Figure 3.24 provides information about the membranes response near the crown. In particular, the pressure-stretch data is shown in Figure 3.24A. The membrane starts from an undeformed state (λ_0 =1) and reaches to a stretch ratio of near λ_0 =2.2 at about p =4.15 kPa. Moreover, it can be seen from Figure 3.47B that the curvature initially increases up to about p =3.2 kPa and then snaps back and decreases thereafter. It can also be seen that despite the larger pressure ranges experienced in this case, the crown stress (Figure 3.24C) is smaller than that of a uniform thickness membrane since the crown's stretch ratio is smaller here and the membrane is thicker at the center.

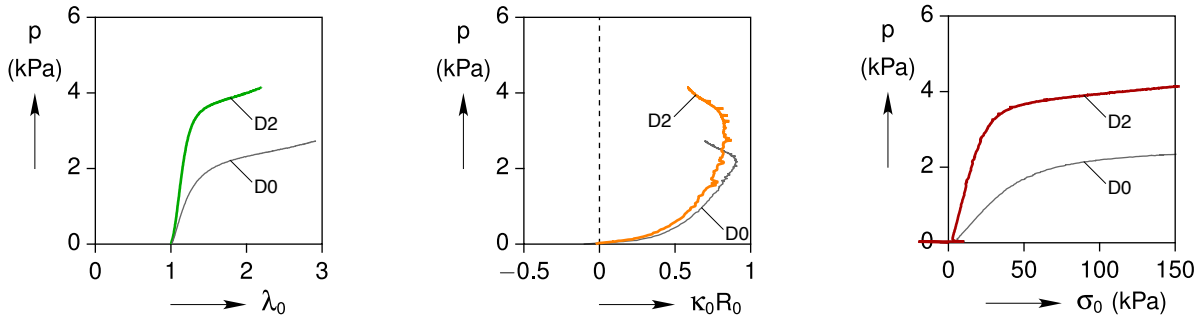

A. pressure-stretch B. pressure-curvature C. pressure-stress

Figure 3.24: Measured crown data of the nonuniform membrane (distribution D2).

The variation of the two principal stretch ratios, λ_R and λ_Θ, in the radial and hoop directions, respectively, are plotted at the time of maximum inflation as a function of R/R_0 in Figure 3.25. By comparing the two principal stretch ratios, we can see that for a circular membrane with radially decreasing thickness, at each radius, λ_R is greater than λ_Θ, except

for the crown, where the two stretch ratios are equal (Figure 3.25C). Moreover, it can be seen that λ_Θ monotonically decreases to the value of one at the clamped boundary ($\lambda_\Theta = 1$), while λ_R monotonically increases moving from the crown towards the edge. This is in contrary to the two previous cases and explains that the membrane gets more stretched in the meridian direction close to the clamped boundary compared to the crown, since it is much thinner near the edge. Similar to the previous cases, the state of stress, changes from equi-biaxial tension at the crown (Equation (3.5)) to pure shear (Equation (3.4)) at the edge, for a nonuniform membrane with thickness distribution D2.

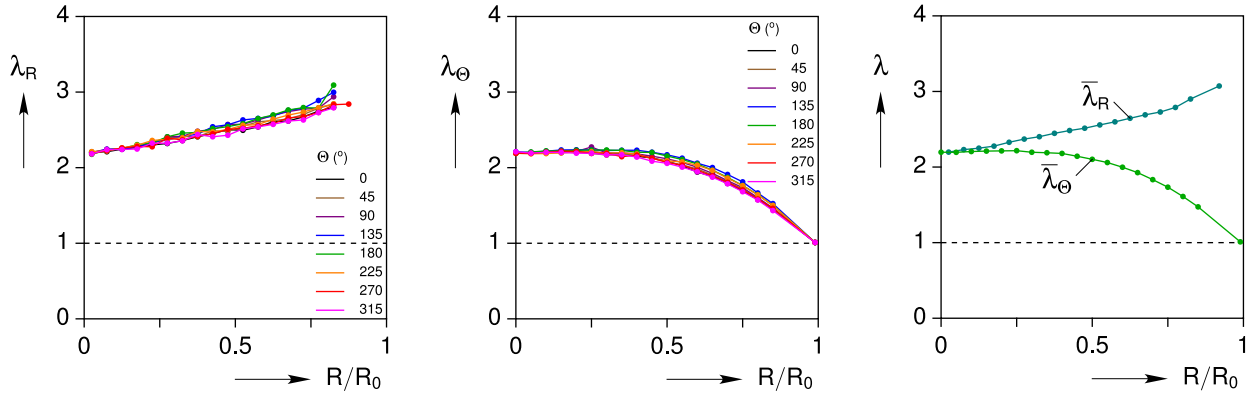

A. Radial stretch B. Hoop stretch C. Θ-averaged

Figure 3.25: Radial distributions of the two principal stretches in the nonuniform membrane (distribution D2) at the time of maximum inflation.

The dimensionless deformation profile history of the inflated membrane at selected instants of time are depicted in Figures 3.26A and 3.26B in two planes cutting through the membrane, namely the X-Z and Y-Z planes. It can be seen that, compared to the uniform thickness membrane, the deformation profiles are more flattened in this case. In addition to the deformation profiles, the position history of the dots during the inflation processes, are demonstrated in these plots. It is observed that the dot at the crown ($X = Y = 0$) deforms almost only vertically in the Z direction, while all other dots deform both in radial and vertical directions.

Viewed from above the membrane, the deformation histories of the crown and eight equally spaced dots around the crown are shown in Figure 3.27. The figure suggests that the deformation is not completely axisymmetric, as it is supposed to be, an leans slightly towards one positive X direction.

Variations of the invariants of the left Cauchy-Green deformation tensor in terms of $I_1 - 3$ and $I_2 - 3$ contour plots are shown in Figure 3.28, respectively.

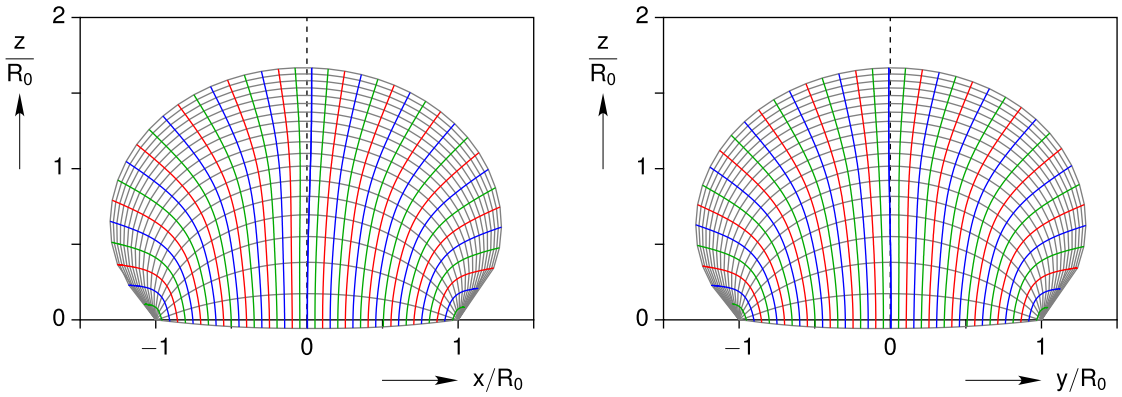

A. $Y = 0$ plane B. $X = 0$ plane

Figure 3.26: Measured deformation profiles (gray lines) and displacement histories of dots (colored lines) during inflation of the nonuniform membrane (distribution D2).

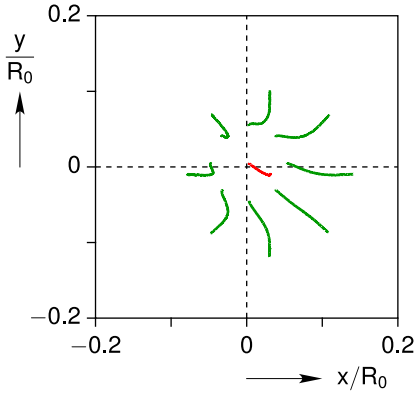

Figure 3.27: Plan view of the displacement history of the crown (red) and the eight adjacent dots (green) during inflation of the nonuniform membrane (distribution D2).

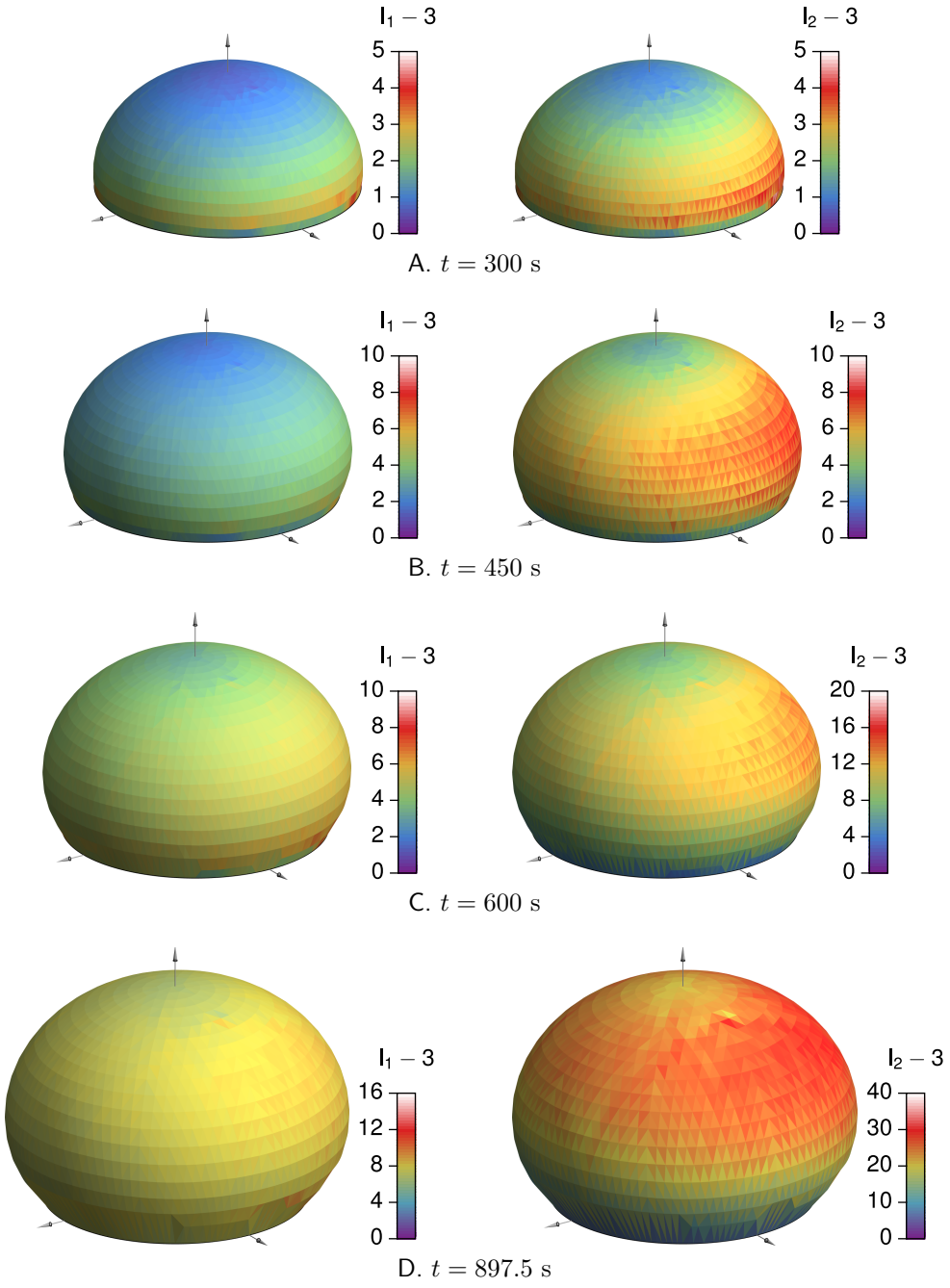

Figure 3.28: Measured contours of $I_1(\boldsymbol{B})$ and $I_2(\boldsymbol{B})$ for the nonuniform membrane (distribution D2).

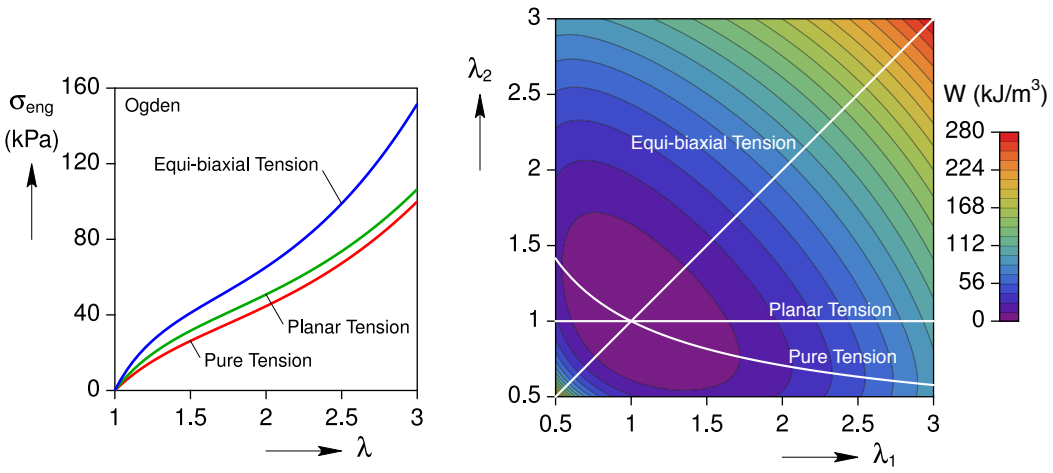

A. Constitutive response B. Strain energy density contours

Figure 3.29: The Ogden constitutive behavior for Ecoflex 00-30 silicone rubber. (A) response to simple constitutive tests and (B) contours of strain energy density.

3.4.4 Axisymmetric simulation results

The numerical results are obtained via the finite-element analysis. Depending on the nature of the problem, either continuum or membrane elements are used. First we examine the accuracy of the finite-element (FE) model, by comparing the experimental results of the uniform membrane inflation with the predicted responses of the FE model. Next a parametric study is carried out to investigate the effect of the nonuniformity in geometrical distribution on the response and stability of axisymmetric membranes.

Validation with experimental data: To achieve a solid foundation for a numerical parametric study, we first validate the FEA results with the experimentally measured data. For this purpose, we use the nonlinear least-squares fit results of Table 3.2, to approximate the constitutive behavior of the rubber material with the Ogden's hyperelastic energy density function. As shown in Figure 3.29A, the constitutive behavior of the Smooth-On's Ecoflex 00-30 silicone rubber, are re-plotted in terms of stretch-stress responses to pure tension, planar tension, and equi-biaxial tension experiments. The contours of constant energy density (W) in the λ_1-λ_2 space are also plotted in Figure 3.29B. Such a plot gives a sense for the range of accuracy the Ogden's model based on the amount of stretch ratios experienced during any experiment. For example, a contour line that crosses the pure tension curve at λ_1 =2.55, will cross the planar tension curve at λ_1 =2.43, and equi-biaxial tension test at λ_1 =1.82. This implies that an Ogden's model that is obtained only but fitting the model to a pure tension test up to stretch ratio of λ_1 =2.55, might predict accurate results only if the equi-biaxial stretches during the membrane inflation experiment are below $\lambda_1 = \lambda_2$ =1.82. The Ogden

coefficients used here (listed in Table 3.2), however, are obtained by a simultaneous fit up to stretch ratio of λ_1 =2.75 in all the constitutive tests.

Figure 3.30 presents a comprehensive comparison of the accuracy of the FEA with the adopted Ogden's hyperelastic coefficients versus the experimentally measured data. In particular, the deformation profiles at multiple instants of time are compared in Figure 3.30A and very good agreements are observed between the FE and experimental results. Very good agreements are also observed in the pressure-curvature (Figure 3.30B) and pressure-stretch (Figure 3.30C) responses at the the crown. The pressure-volume response of the membrane (Figure 3.30D) also shows a very good agreement between FEA and experimental data. Comparison of the principal stretch ratios along the radius of the membrane, at the time of maximum inflation, also demonstrates a good agreement, although the FE results in general slightly over predicts the stretch ratio values (Figures 3.30E and 3.30F).

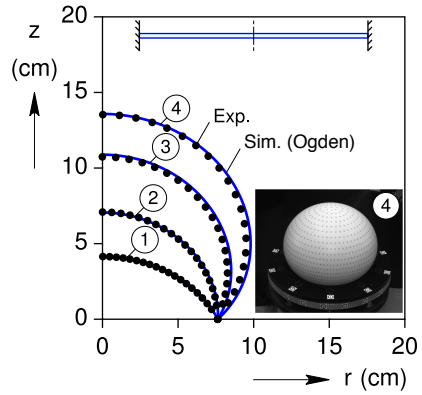

A. Deformed profiles

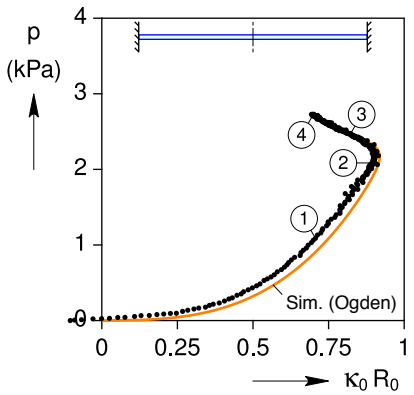

B. Pressure-crown curvature

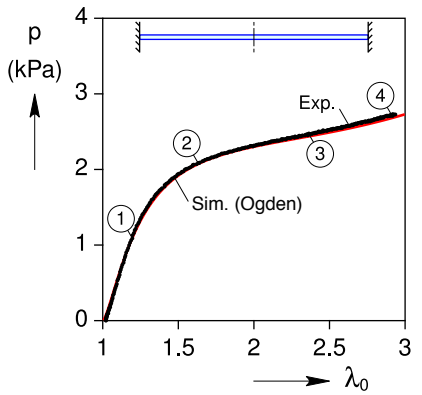

C. Pressure-crown stretch

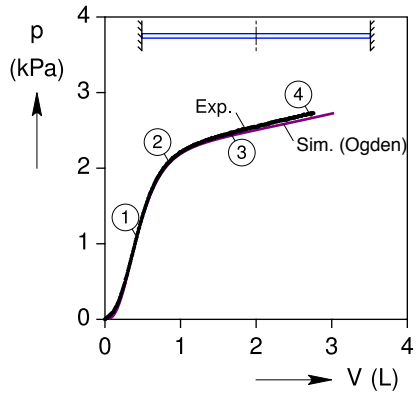

D. Pressure-volume

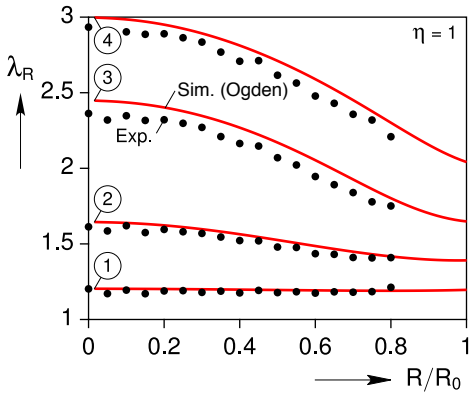

E. Radial stretch

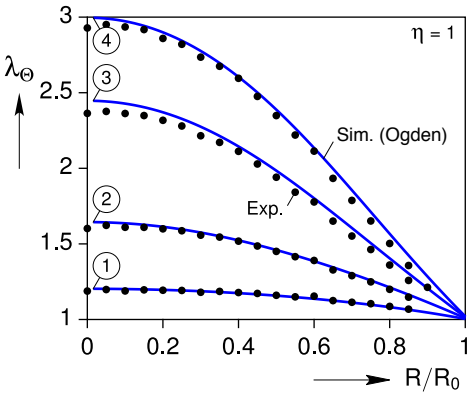

F. Hoop stretch

Figure 3.30: Comparison of experimental data and FEA predictions for the uniform membrane.

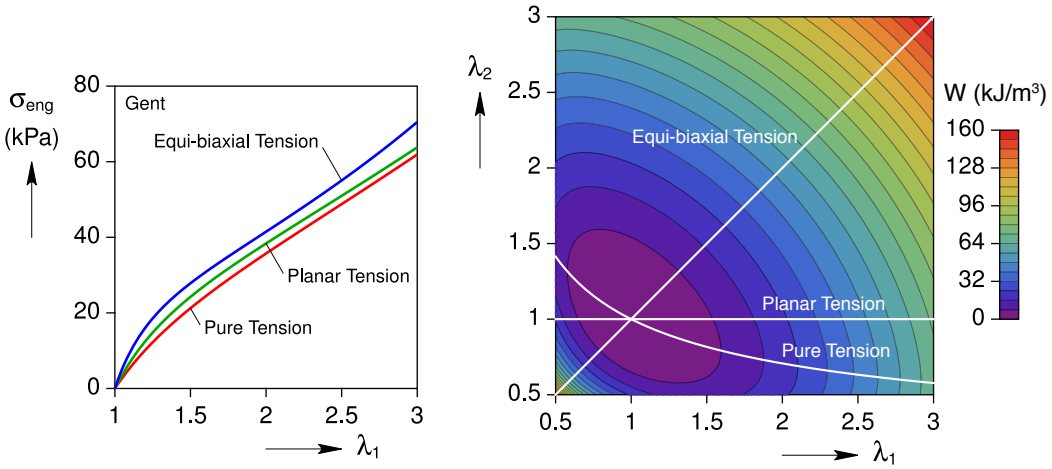

A. Constitutive response B. Strain energy density contours

Figure 3.31: The Gent strain energy density function with $c_1 = 10$ kPa and $J_m = 100$. (A) response to simple constitutive tests and (B) contours of strain energy density.

Numerical parameter study: A finite-element parametric study through using axisymmetric membrane elements is carried out here to investigate the effect of geometric nonuniformities on the response of an axisymmetric circular membrane. The Gent energy density function with arbitrarily chosen values of c_1 =10 kPa and J_m =100 is considered for this study (Figure 3.31). Moreover, for simplicity the following non-dimensioalized parameters are introduced

$$\overline{V} = \frac{V}{R_0^3}, \; \overline{p} = \frac{pR_0}{E_0 h_{avg}} \tag{3.8}$$

where $\overline{V}$ is the dimensionless volume and $\overline{p}$ is the dimensionless pressure. Also, E_0 is small strain Young's modulus defined as $E_0 = 3\mu_0$ and $h_{avg} = (h_0 + h_1)/2$ is the average thickness of the membrane. It is important to mention that for comparison purposes, the material volume of the circular membrane itself is kept constant and equal to the material volume of the uniform thickness membrane, regardless of thickness ratio value, η.

The variations in crown's stretch ratio versus the changes in pressure are plotted in Figure 3.32 for the three thickness distribution cases. The pressure-stretch plot shows an up-down-up behavior in the uniform thickness distribution case (distribution D0), corresponding to a limit-point structural instability in the response (Figure 3.32A). The unstable region of the equilibrium path which occurs approximately between the crown stretch ratios of λ_0 =2.5 and λ_0 =4.5 is dashed, for demonstration purposes. For a nonuniform thickness membrane with distribution D1 and $\eta = h_1/h_0$ =5, the pressure-stretch ratio diagram (Figure 3.32B) does not show any limit-point instability in the response and the pressure

monotonically increases as the stretch ratio of the crown increases. For a nonuniform thickness membrane with distribution D2 and $\eta = h_1/h_0 = 1/5$, the pressure-stretch ratio diagram (Figure 3.32C) again shows a limit-point instability in the response approximately between the crown stretch ratios of λ_0 =1.6 and λ_0 =3.35. Also, compared to the uniform distribution case, in distribution D2, the instability begins at a smaller dimensionless pressure and crown stretch. In addition, the length of the unstable region along the pressure-stretch equilibrium path is smaller in distribution D2 and the up-down-up behavior is more pronounced. Moreover, comparing the three distributions, we can see that the crown stretch ratio of distribution D1 is always higher that the other two cases at any given dimensionless pressure.

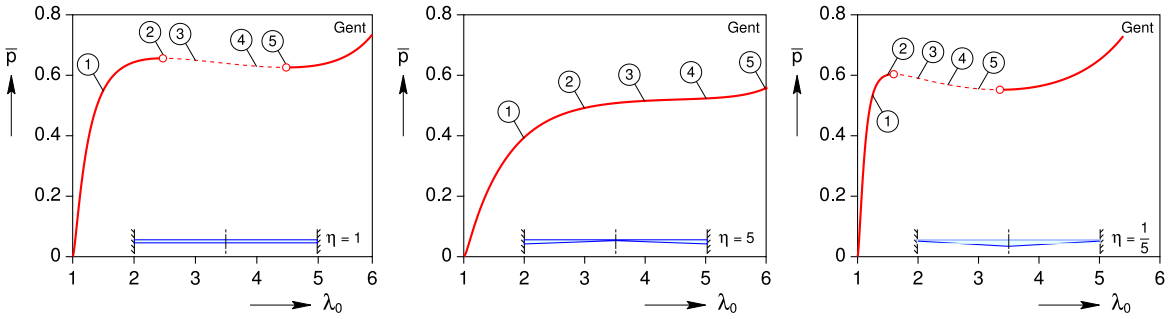

A. Distribution D0 B. Distribution D1 C. Distribution D2

Figure 3.32: Calculated pressure-crown stretch responses for three membrane thickness distributions of the same material volume.

The deformation profiles of the three thickness distribution cases are compared in Figure 3.33 at different stretch ratios. For the uniform distribution case, the deformation profiles are plotted at crown stretch ratios λ_0 =1.5, 2.5, 3.0, 4.0, and 4.5 as labeled with circled numbers 1 to 5, respectively, in its corresponding pressure-stretch plot of Figure 3.32A. The deformation profiles of the nonuniform membrane with thickness distribution D1, are plotted at crown stretch ratios λ_0 =2.0, 3.0, 4.0, 5.0, and 6.0 as labeled with circled numbers 1 to 5, respectively, in its corresponding pressure-stretch plot of Figure 3.32B. For the nonuniform membrane with thickness distribution D2, the deformation profiles are plotted at crown stretch ratios λ_0 =1.25, 1.5, 2.0, 2.5, and 3.0 as labeled with circled numbers 1 to 5, respectively, in its corresponding pressure-stretch plot of Figure 3.32C. By comparison of the deformation profiles of the three cases at λ_0 =3, as labeled by 3, 2, and 5 in the distributions 0, 1, and 2, respectively, the membrane with distribution D2 would achieve a much larger deformation profile in order to reach the same crown stretch.

Figure 3.34 represents the changes in the pressure-volume response of the three thickness distributions. Similar behavior to the crown's pressure-stretch response is observed here. It

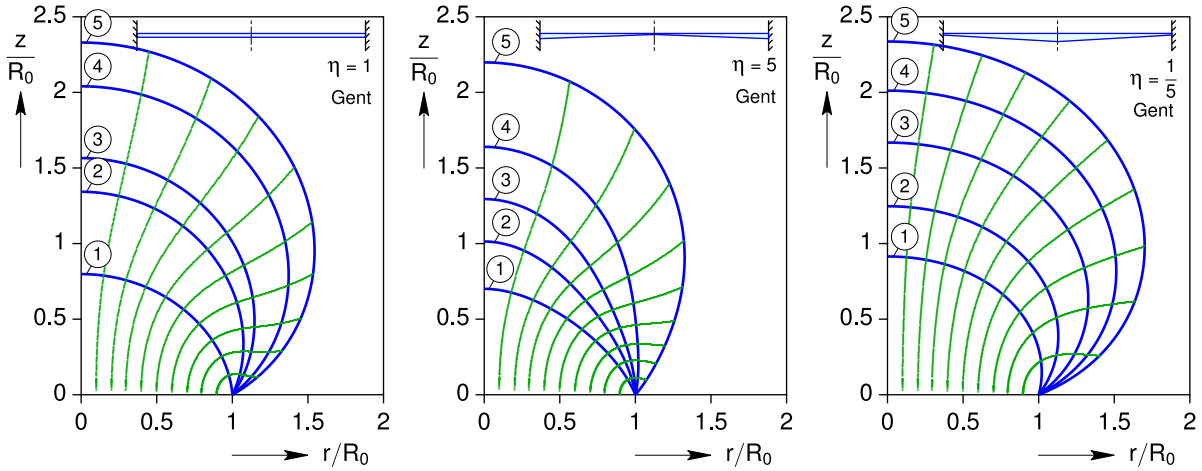

A. Distribution D0 B. Distribution D1 C. Distribution D2

Figure 3.33: Calculated membrane profiles (blue) and point histories (green) for three membrane thickness distributions.

can be seen that compared to a uniform thickness membrane, the up-down-up behavior of the pressure-volume response is deeper in distribution D2 and the unstable region covers a larger volume change.

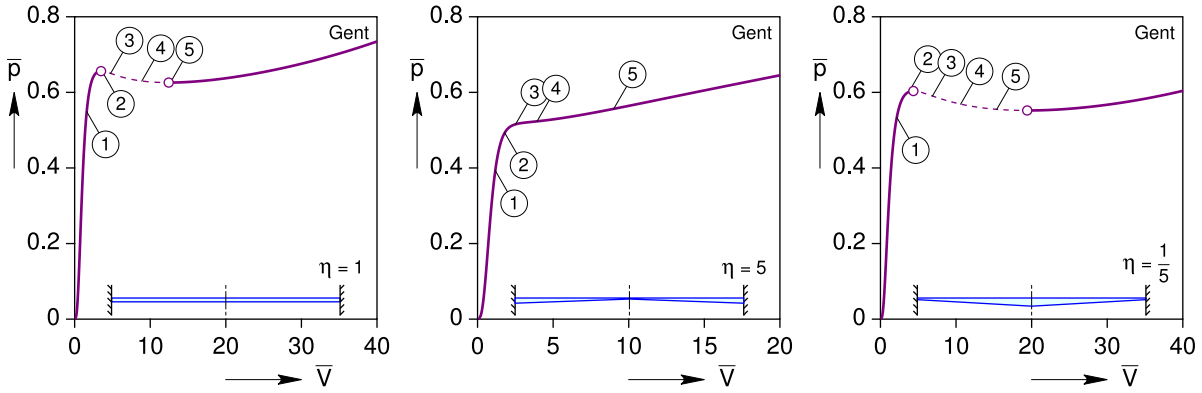

A. Distribution D0 B. Distribution D1 C. Distribution D2

Figure 3.34: Calculated pressure-volume responses for three thickness distributions.

The changes in the two principal stretch ratios of the membrane with respect to the radius in the undeformed configuration are demonstrated in Figure 3.35 for the three thickness distribution cases. It can be seen that the principal stretch ratio in the circumferencial direction, λ_θ, is always equal to one at the edge of the membrane (pure shear state of stress). Moreover, for distributions 0 and 2, λ_r (in the meridian direction) is larger than λ_θ, everywhere along the radius, however, this behavior is not observed in distribution D1. Furthermore, for distributions 0 and 1, λ_r monotonically decreases moving towards the edge

of the membrane, but it increase in the case of distribution D2.

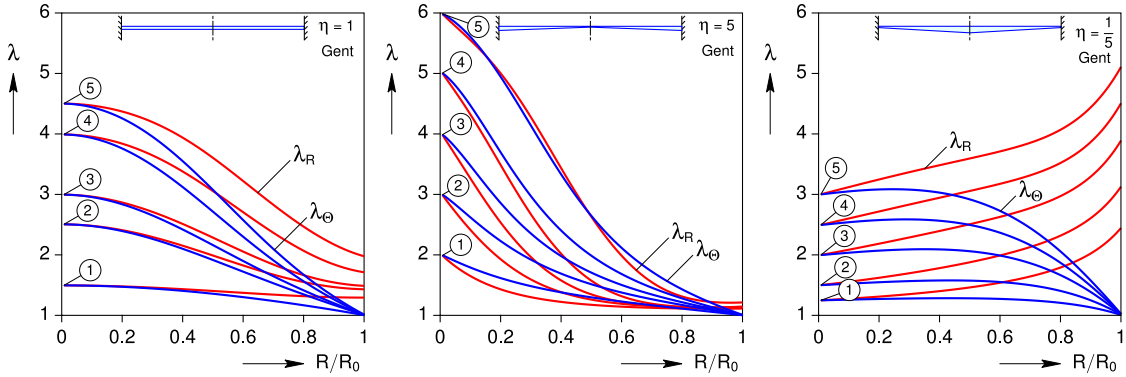

Figure 3.35: Calculated pressure-crown stretch profiles for three thickness distributions.

In addition to the above comparison between the three distributions, we can also examine the effect of the edge to center thickness ratio, η, on the response of nonuniform thickness axisymmetric membranes. Figure 3.36, demonstrates the pressure-volume and crown's pressure-stretch response of the membrane with thickness distribution D1. It can be seen from the responses that for a uniform thickness membrane (η=1) that demonstrates structural instability in its pressure response, the instability can be avoided and the curves can be flattened if η is increased.

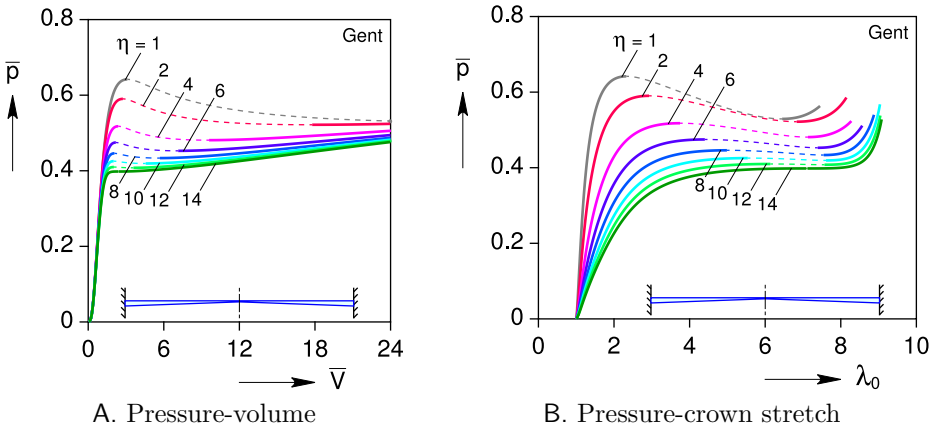

Figure 3.36: The effect of increasing thickness slope (η) on the response of an axisymmetric membrane.

A similar study on the effect of edge to center thickness ratio on the pressure response of a membrane with thickness distribution D2, can also be performed, as shown in Figure 3.37. It is observed that for a uniform thickness membrane (η=1) that demonstrates structural

instability in its pressure response, the instability can be pronounces and forced to happen earlier if η is decreased.

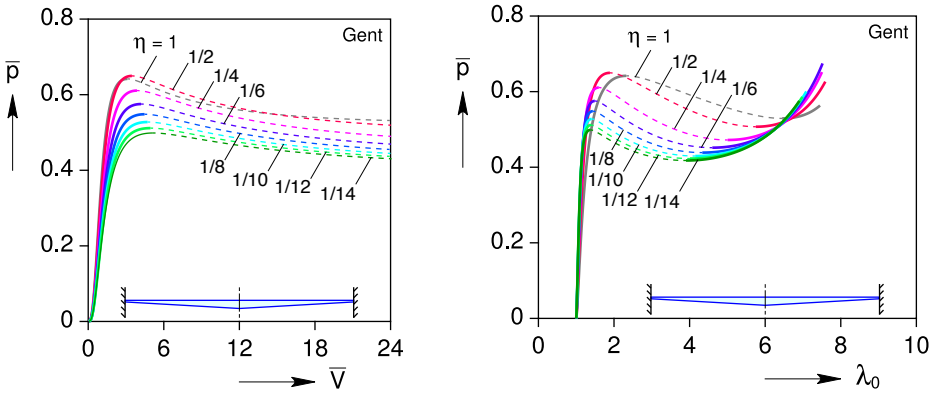

A. Pressure-volume B. Pressure-crown stretch

Figure 3.37: The effect of decreasing thickness slope (η) on the response of an axisymmetric membrane.

Finally, the responses of the three distribution cases are summarized and compared together in three representative plots, crown's pressure-stretch (Figure 3.38B), pressure-volume (Figure 3.38A), and deformation profile (Figure 3.38C). The thickness ratio is set to $\eta = 5$ for distribution D1 and $\eta = 1/5$ for distribution D2, in Figure 3.38.

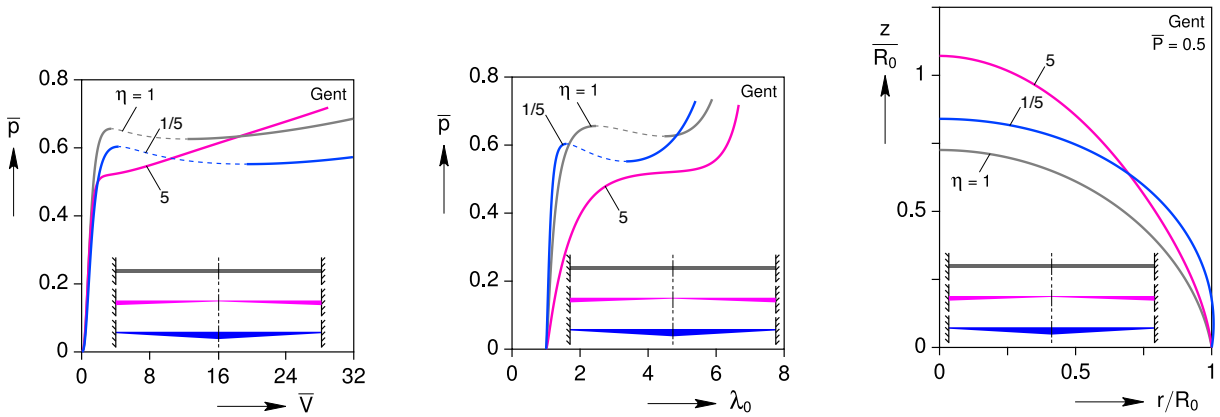

A. Pressure-volume B. Pressure-crown stretch C. Deformations

Figure 3.38: Comparison of inflation responses of the three thickness distributions.

3.5 Non-axisymmetric inflation

In this section, we present the experimental results of three non-axisymmetric inflation cases. These include a circular membrane with diametrically increasing thickness, a uniform

thickness bimaterial membrane, and a uniform thickness spirally reinforced membrane. The pressure response of each membrane is investigated and the deformation profiles with their corresponding kinematic 3D contour plots are extracted using photogrammetry.

3.5.1 Distribution D3 (diametrically increasing thickness)

The experimental results of the first non-axisymmetric case, a circular membrane with increasing thickness across the diameter (wedge-like) made of EF30, are presented here. The membrane's thickness is considered to linearly increase in the positive X direction (thickness distribution D3).

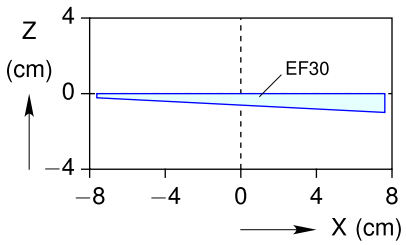

A. Membrane cross-section

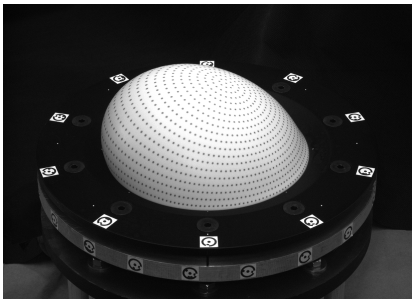

B. $t = 240$ s

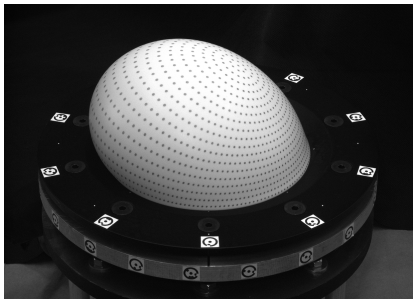

C. $t = 360$ s

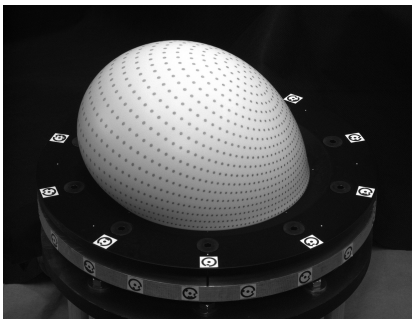

D. $t = 480$ s

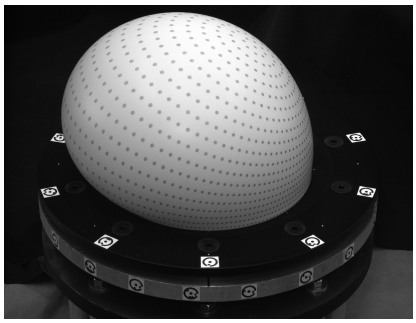

E. $t = 718$ s

Figure 3.39: Photographs of the nonuniform thickness membrane (distribution D3) at selected times during inflation.

The membrane was fabricated using a constant depth mold which was tilted to allow the liquid rubber to flow in the positive X direction before curing, resulting in a linear increase in

the thickness by an amount of 7.62 mm (0.3 in) at $X = 3$ in compared to $X = -3$ in. After the rubber was cured, the thickness was measured to be 2.187 mm (0.0861 in) at $X = -3$ in and 9.957 mm (0.392 in) at $X = 3$ in. Figure 3.39A shows the thickness distribution of the non-axisymmetric membrane of this case. It should be mentioned that $Y = 0$ is the plane of symmetry in this case.

Figures 3.39B–3.39E show snapshots of the membrane viewed from one of the nine cameras, at four instants of time during inflation. Interestingly, the deformed geometry resembles the shape of a 'bike helmet'.

The pressure and volume-change histories during inflation are demonstrated in Figures 3.40A and 3.40B. The pressure-volume cross plot is shown in Figure 3.40C which shows an 'S-shape' behavior similar to the previous axisymmetric cases.

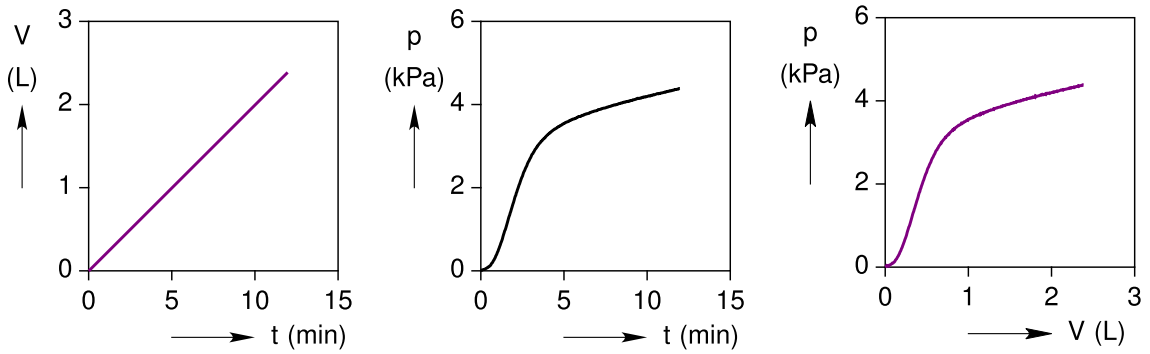

A. Volume history B. Pressure history C. Pressure-volume

Figure 3.40: Pressure and volume data of the nonuniform membrane (distribution D3).

Figure 3.41 provides information about the membrane's response at its center. In particular, the pressure-stretch data is shown in Figure 3.41A. In contrary to the axisymmetric inflation cases, the stretch ratios in the X and Y directions are no longer equal at the center. It's also observed that λ_{0y} and λ_{0x} both increase as the pressure increases, however, λ_{0y} is always greater than or equal to λ_{0x} during inflation. The membrane starts from an undeformed state with $\lambda_{0x} = \lambda_{0y} = 1$, however after pressurization begins, the difference between λ_{0y} and λ_{0x} increases and reaches to its maximum at about $p = 3.0$ kPa. Thereafter, the difference between the two stretch ratios decreases as the membrane gets more ans more inflated until the two stretches merge together at about $p = 4.1$ kPa. The change in curvatures of the membrane's center with pressure is presented in Figure 3.41B. As expected, because of the non-axisymmetric response of the inflation, the curvatures in the X and Y directions are not equal. It can be seen that the change in both curvatures are nonmonotonic. Specifically, κ_{0y} shows the same overall behavior as the previous axisymmetric cases, however, κ_{0x} , although

initially similar to κ_{0y}, starts deviating from κ_{0y} at about p =1 kPa and demonstrates a completely different trend afterwards.

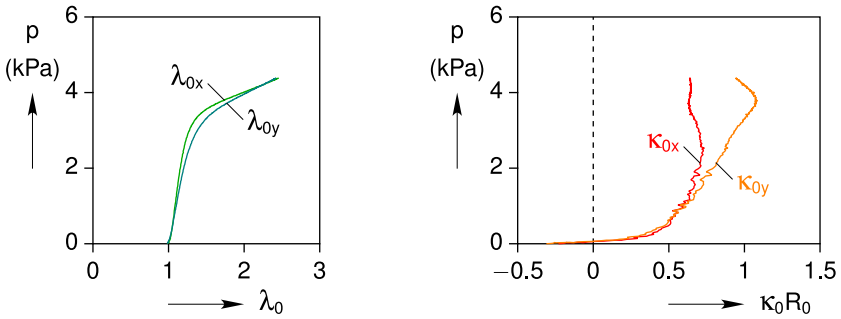

A. Pressure-stretch B. Pressure-center curvature

Figure 3.41: Measured data at the nonuniform membrane (distribution D3) center.

The variation of the radial and hoop stretch ratios, λ_R and λ_Θ, at eight equally spaced radial directions around the center of the membrane, are plotted at the time of maximum inflation as a function of dimensionless radius (R/R_0) of the undeformed configurations in Figure 3.42. It should be mentioned that $\theta = 0°$, $\theta = 90°$, $\theta = 180°$, and $\theta = 270°$, correspond to the positive X direction, positive Y direction, negative X direction, and negative Y direction, respectively. Also, it is worth noticing that λ_R corresponds to λ_x at $\theta = (0°, 180°)$, and corresponds to λ_y at $\theta = (90°, 270°)$.

The decrease in λ_R from the center towards the edge for $\theta = 0°$ is similar to the behavior observed in the distribution D1 of the axisymmetric cases, as the membrane becomes thicker towards the positive X direction. Similarly, the increase in λ_R from the center towards the edge for $\theta = 180°$ is similar to the behavior observed in the distribution D2 of the axisymmetric cases, as the membrane becomes thinner towards the negative X direction. Moreover, since the membrane is symmetric with respect to the Y-plane, for the pairs $\theta = (45°, 315°)$, $\theta = (90°, 270°)$, and $\theta = (135°, 225°)$, the variations in both λ_R and λ_Θ naturally come out to be coinciding. Furthermore, as can be seen in Figure 3.42B, λ_Θ, for all directions, reaches to the value of unity the edge, as expected. Interestingly, the λ_Θ at $\theta = (135°, 180°, 225°)$, initially increases in the radial direction and then decreases towards unity.

The dimensionless deformation profile history of the inflated membrane at selected instants of time are depicted in Figures 3.43A and 3.43B in two planes cutting through the membrane, namely the X-Z and Y-Z planes. In addition to the deformation profiles, the position history of the black dots during the inflation processes, are demonstrated in these plots. It is observed that the black dot at the center of the membrane ($X = Y = 0$) deforms vertically in the Z direction as well as horizontally in the positive X direction.

Variations of the invariants of the left Cauchy-Green deformation tensor ($\boldsymbol{B}$) across the

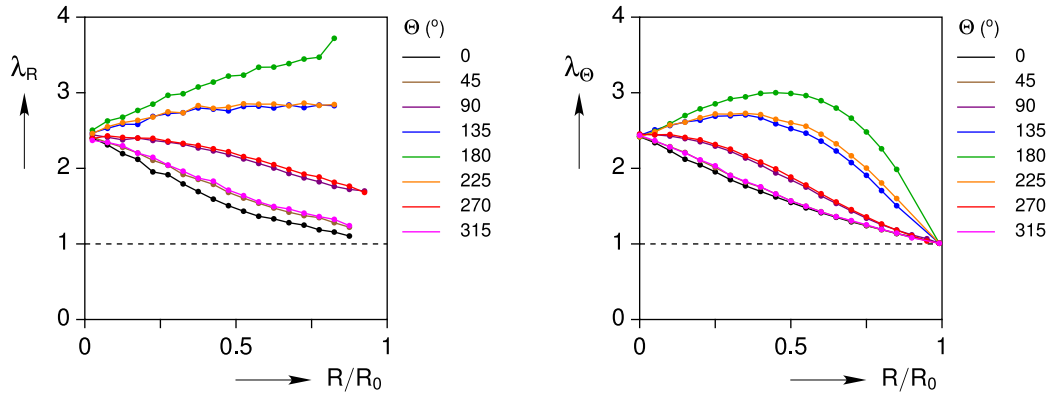

A. Radial stretch profiles B. Hoop stretch profiles

Figure 3.42: Radial distributions of the stretch ratios in the nonuniform membrane (distribution D3) at the time of maximum inflation.

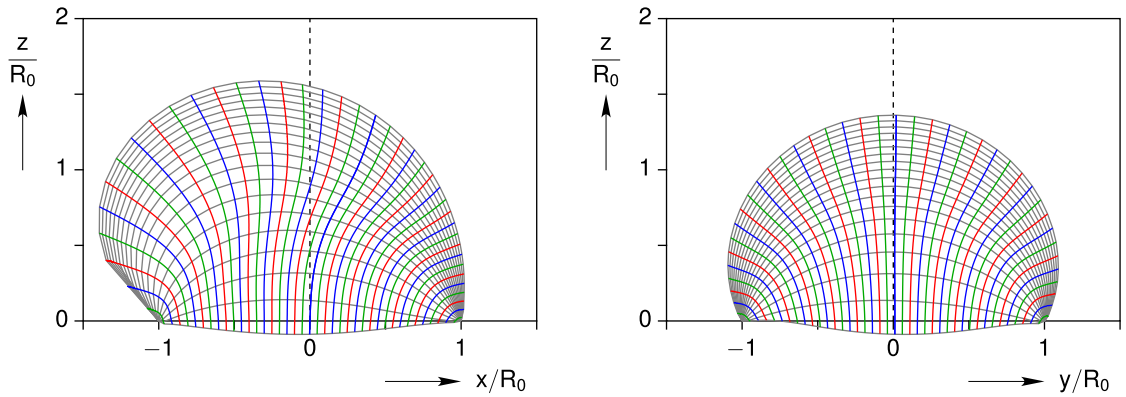

A. $Y = 0$ plane B. $X = 0$ plane

Figure 3.43: Measured deformation profiles (gray lines) and displacement histories of dots (colored lines) during inflation of the nonuniform membrane (distribution D3).

surface of the membrane are studied next. Figure 3.44 present the 3D contour plots of the quantities $I_1 - 3$ and $I_2 - 3$, respectively, on the deformed configuration at different time frames.

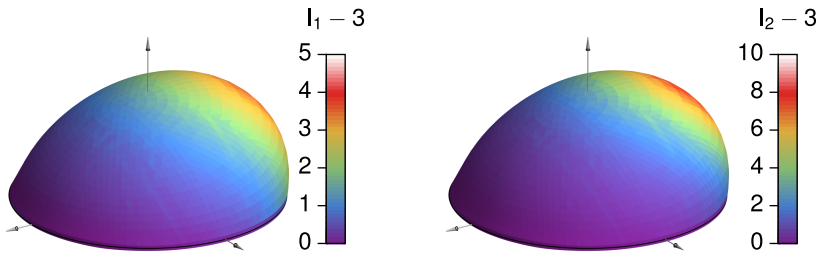

A. $t = 240$ s

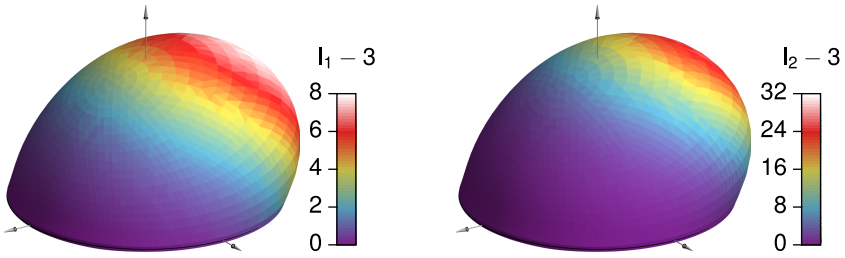

B. $t = 360$ s

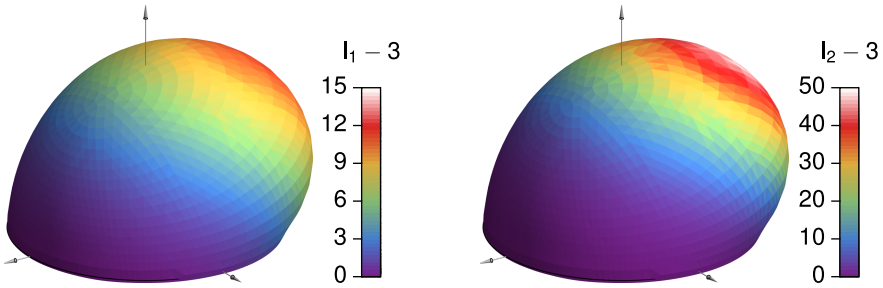

C. $t = 480$ s

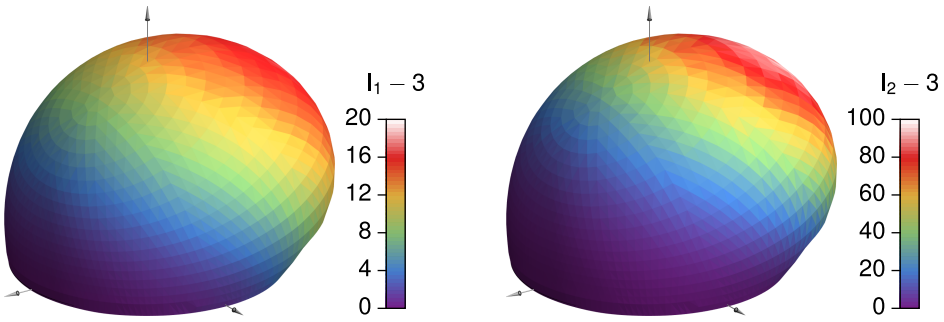

D. $t = 718$ s

Figure 3.44: Measured contours of $I_1(\boldsymbol{B})$ and $I_2(\boldsymbol{B})$ for the nonuniform membrane (distribution D3).

3.5.2 Bimaterial membrane with uniform thickness

The experimental results of the second non-axisymmetric case, a circular membrane with uniform thickness composed of two materials, are presented here. The bimaterial membrane is composed of relatively stiff DragonSkin 00-20 (DS20) material in a central strip within -3.05 cm $\leq X \leq 3.05$ cm (-1.2 in $\leq X \leq 1.2$ in) and softer EF30 material within the remaining side sectors (Figures 3.45A and 3.45B). Documentation from the material supplier indicates that DS20 is about 5 times stiffer than EF30. In this sample, although not axisymmetric, $X = 0$ and $Y = 0$ are planes of symmetry.

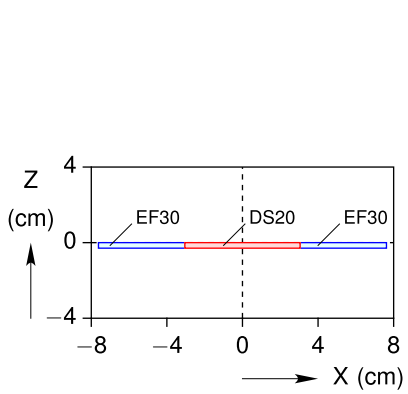

A. Membrane cross-section

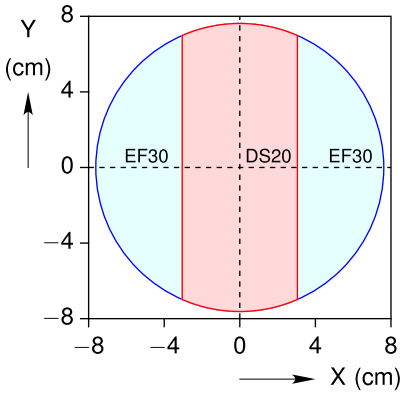

B. Plan view schematic

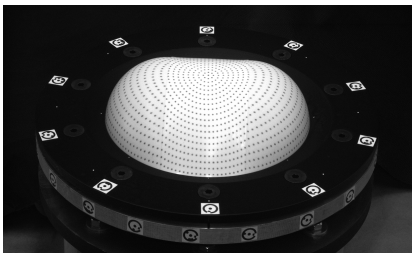

C. $t = 150$ s ($p = 3.05$ kPa)

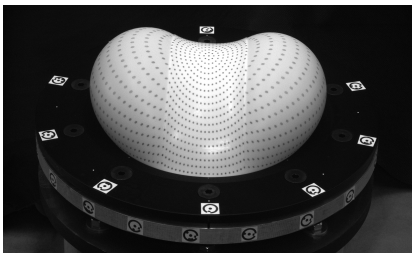

D. $t = 300$ s ($p = 4.95$ kPa)

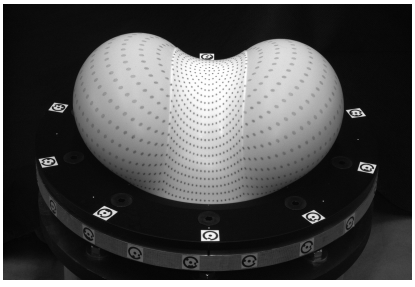

E. $t = 450$ s ($p = 5.89$ kPa)

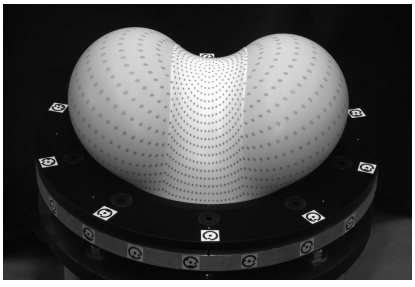

F. $t = 650$ s ($p = 5.86$ kPa)

Figure 3.45: Photographs of the bimaterial membrane at selected times during inflation.

The bimaterial membrane was fabricated using a uniform depth mold in two steps. First,

the two side sectors were made by placing an acrylic insert, with the same shape and dimensions of the stiff segment, in the middle of the mold and pouring the soft EF30 liquid silicone into the open space of the mold. After the side sectors were cured, the insert was removed from the mold and liquid silicone rubber of the stiff DS20 material was poured to fill the space between the side segments. This was allowed to cure resulting in the two materials being bonded together. The initial thickness of the membrane was measured to be 2.921 mm (0.115 in) on average across the membrane.

This bimaterial membrane was designed to explore whether or not inflated membranes could be used to create smooth shapes with negative Gaussian curvatures. The Gaussian curvature is defined as the product of the two principal curvatures, $K = \kappa_1\kappa_2$, so a negative value corresponds to points with saddle-like surfaces. Figures 3.45C–3.45F show snapshots of the membrane viewed from one of the nine cameras, at four instants of time during inflation. As inflation progressed the deformed profile of the membrane developed into the shape of a 'saddle' or 'bean', demonstrating that a negative Gaussian curvature is indeed feasible. The stiffer material played the role of a constraining 'strap' that suppressed the deformation along the Y-axis ($X = 0$) while the softer material bulged outward.

The pressure and volume-change histories during inflation are provided in Figures 3.46A and 3.46B, and the pressure-volume cross-plot is shown in Figure 3.46C. Interestingly, the pressure increases up to about p =6.1 kPa at $t = 8.8$ min, where it reaches a limit pressure and then decreases thereafter. If the pressure had been controlled (rather than the inflation volume), this limit pressure would have initiated an instability. It is unclear if this would have been arrested at higher inflation volumes. The experiment was terminated at $V = 2.17$ L to avoid breaking the bond between the two materials and bursting the membrane.

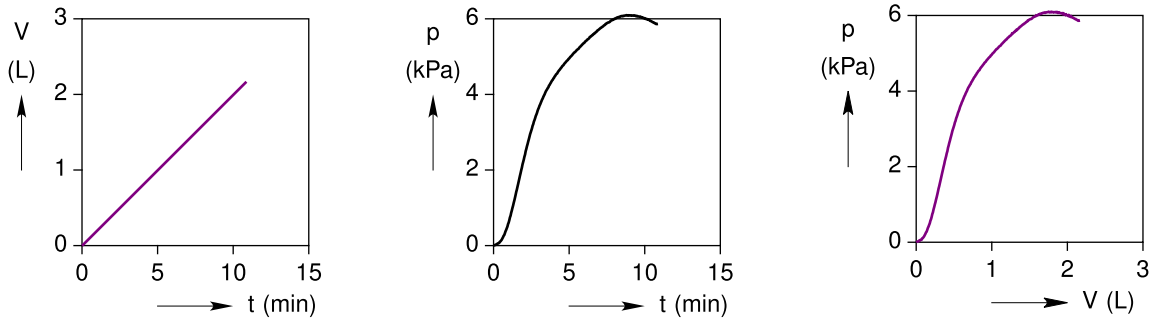

A. Volume history B. Pressure history C. Pressure-volume

Figure 3.46: Structural response of the bimaterial membrane.

The pressure response at the center of the membrane is demonstrated in Figure 3.47. Figure 3.47A provides the pressure-stretch data at the center of the membrane, showing the

evolution of $\lambda_{0x} < 1$ and $\lambda_{0y} > 0$ during inflation. Since $X = 0$ and $Y = 0$ are symmetry planes, the principal stretch ratios at the membrane center are in fact $\lambda_1 = \lambda_{0x}$ and $\lambda_2 = \lambda_{0y}$ and the principal curvatures are $\kappa_1 = \kappa_{0x}$ and $\kappa_2 = \kappa_{0y}$. As can be seen from the snapshots of the deformation and verified in Figure 3.47B, the Gaussian curvature of the membrane's center is positive during the early stages of the inflation, since both κ_{0x} and κ_{0y} are initial positive. At about $p = 2.2$ kPa, the Gaussian curvature becomes zero when κ_{0x} decreases to zero. Subsequently, the Gaussian curvature becomes negative as κ_{0x} becomes negative (and $\kappa_{0y} > 0$), and the deformed profile becomes saddle-shaped.

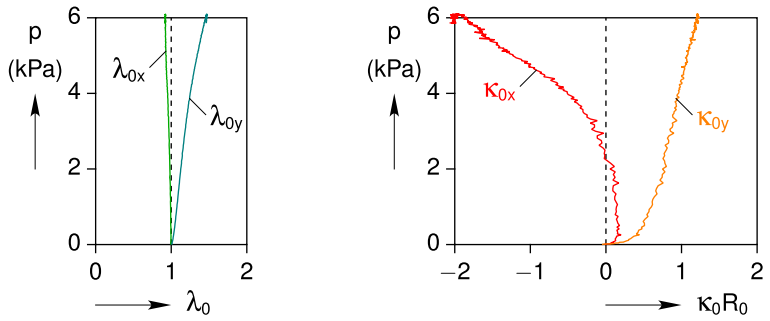

A. pressure-stretch B. pressure-curvature

Figure 3.47: Measured data at the center of the bimaterial circular membrane.

The question arises whether the stress σ_{0x} is compressive, since $\lambda_{0x} < 1$ occurs throughout the inflation. The answer is no, the stress is tensile ($\sigma_{0x} > 0$), despite the negative curvature ($\kappa_{0x} < 0$) that occurs at large pressures. No wrinkling is observed near the center, which suggests that either the finite (but small) membrane thickness has enough bending stiffness to suppress local buckling or the stress is indeed positive. A magnified view of the center stretch ratios is shown in Figure 3.48, along with a dashed line showing a hypothetical $\lambda_{0x}^{\text{hyp}} = \lambda_{0y}^{-1/2}$ based on the measured λ_{0y} data as if $\sigma_{0x} = 0$, i.e., pure tension in the Y direction. Since this hypothetical stretch ratio is always less than the measured λ_{0x} and the material behavior is isotropic, the actual stress σ_{0x} must be slightly positive to pull the stretch ratio up its measured value. Furthermore, the equilibrium relation normal to the membrane is

$$h\,\kappa_1\,\sigma_1 + h\,\kappa_2\,\sigma_2 = p, \tag{3.9}$$

where $h = \lambda_3 h_0 = \lambda_1^{-1}\lambda_2^{-1} h_0$ is the current membrane thickness and σ_1 and σ_2 are the principal Cauchy stresses. Taking $\sigma_1 = \sigma_{0x} > 0$, $\sigma_2 = \sigma_{0y} > 0$, $\kappa_1 = \kappa_{0x} < 0$, and $\kappa_2 = \kappa_{0y} > 0$, it is clear that σ_{0y} must be sufficiently larger than σ_{0x} to offset the negative curvature κ_{0x} to maintain the positive pressure $p > 0$. Hence, the stress state is unequal biaxial tension $\sigma_{0y} > \sigma_{0x} > 0$, but the individual stresses are unknown and would require a

constitutive model to quantify them.

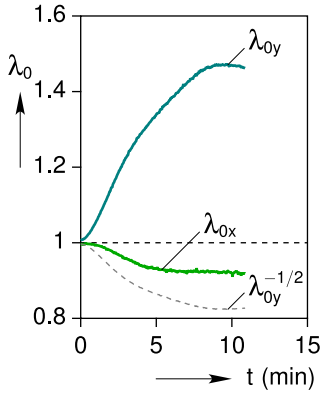

Figure 3.48: Histories of the stretch ratios at the bimaterial membrane center. The gray dashed line shows a hypothetical $\lambda_{0x} = \lambda_{0y}^{-1/2}$ that would make $\sigma_{0x} = 0$.

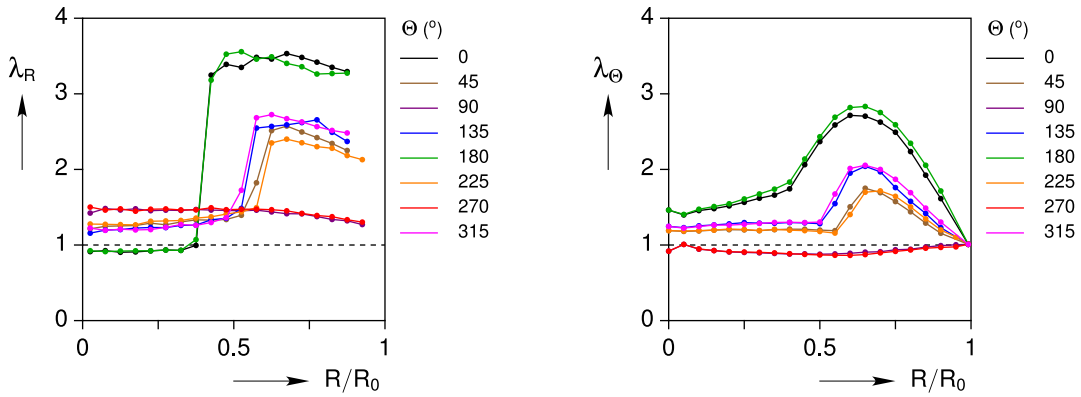

Figure 3.49: Radial distributions of the stretch ratios in the bimaterial membrane at the time of maximum inflation.

The radial distributions of the radial and circumferential stretch ratios, λ_R and λ_Θ, are plotted at the time of maximum inflation in Figure 3.49. It can be seen that both λ_R and λ_Θ have smooth variations in $\theta = (90°, 270°)$ directions, which is merely composed of the stiff segment. For all other selected radial directions, we observe a jump in the magnitude of both λ_R and λ_Θ, as the interface of the two materials is passed. This is due to the fact that as the interface is passed, the material becomes softer and therefore, the stretches become greater. For $\theta = (0°, 180°)$, which coincide with the directions of the material discontinuity, this jump is observed at the dimensionless radius of R/R_0 =0.4 as expected. Also as demonstrated in Figure 3.49A, for $\theta = (0°, 180°)$, λ_R starts from a value slightly smaller than one, λ_R =0.92. Moreover, as can be seen in Figure 3.42B, λ_Θ, for all directions, eventually reaches to the value of unity the edge, as expected.

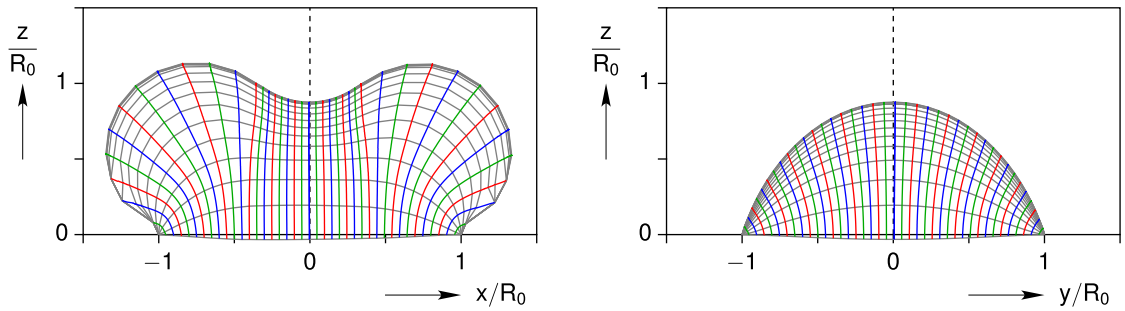

A. $Y = 0$ plane B. $X = 0$ plane

Figure 3.50: Measured deformation profiles (gray lines) and displacement histories of dots (colored lines) during inflation of the bimaterial membrane.

The dimensionless deformation profile history of the inflated membrane at selected instants of time are depicted in Figures 3.50A and 3.50B in two planes cutting through the membrane, namely the X-Z and Y-Z planes. From Figure 3.50A, it can be seen that during the inflation, the curvature near the center of the membrane changes sign, from positive at early stages, to zero, and eventually to negative values at larger deformations.

In addition to the deformation profiles, the position history of the black dots during the inflation processes, are demonstrated in these plots. It is observed that the black dot at the center of the membrane ($X = Y = 0$) deforms almost only vertically in the Z direction, while all other dots deform both in radial and vertical directions.

Variations of the invariants of the left Cauchy-Green deformation tensor ($\boldsymbol{B}$) across the surface of the membrane are studied next. Figure 3.51 present the 3D contour plots of the quantities $I_1 - 3$ and $I_2 - 3$ on the deformed configuration at different time frames.

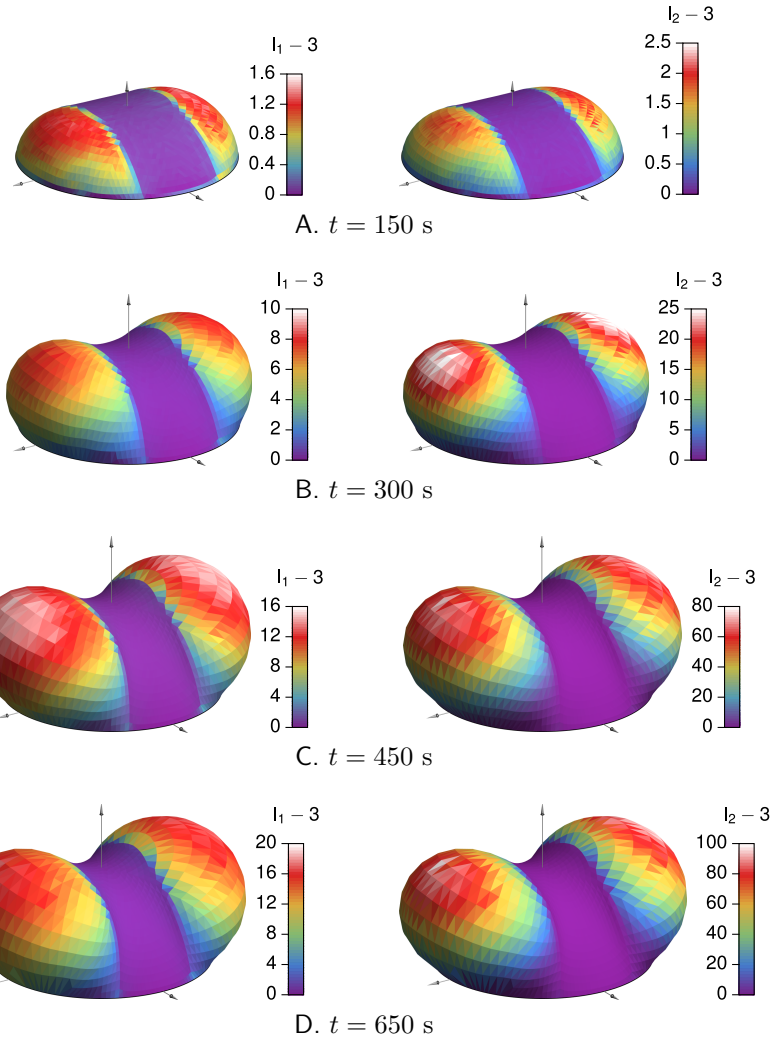

Figure 3.51: Measured contours of $I_1(\boldsymbol{B})$ and $I_2(\boldsymbol{B})$ for the bimaterial membrane.

3.5.3 A spirally reinforced circular membrane with uniform thickness

The experimental results of the third non-axisymmetric case, a uniform thickness circular membrane composed of two materials, a soft matrix (EF30) with stiff spiral fibers (DragonSkin 00-30), are presented here.

The membrane was fabricated using a uniform depth mold in two steps. First, the spiral fibers were made by placing an acrylic sheet insert, with the same shape and dimensions of the soft matrix, in the mold and pouring the stiff DragonSkin 00-30 (DS30) liquid silicone in the open space of the mold. After the fibers were cured, the insert was removed from the mold and the liquid silicone rubber of the soft material (EF30), was poured into the mold to fill the space between the fibers and bond to them. Documentation from the material supplier indicates that DS30 is about 8.6 times stiffer than EF30. Figures 3.52A and 3.52B

show the thickness and material distribution of the non-axisymmetric membrane of this case. The initial thickness of the membrane was measured to be 3.175 mm (0.125 in) on average across the membrane. Also, the fibers were designed to have a width of 1.524 mm (0.06 in) which is equal to 1% of the diameter of the membrane. As can be seen, the membrane has a total of 16 logarithmic spiral fibers with the following parametric description

$$X(t) = 3\,\mathrm{e}^{-t}\cos t, \quad 0 \le t \le \pi \tag{3.10a}$$

$$Y(t) = 3\,\mathrm{e}^{-t}\sin t. \quad 0 \le t \le \pi \tag{3.10b}$$

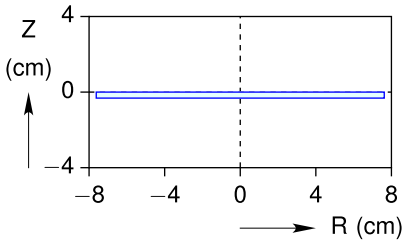

A. Membrane cross-section

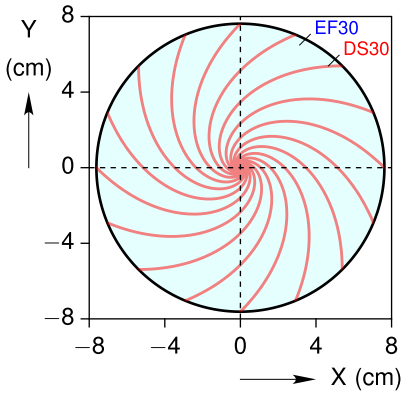

B. Plan view schematic

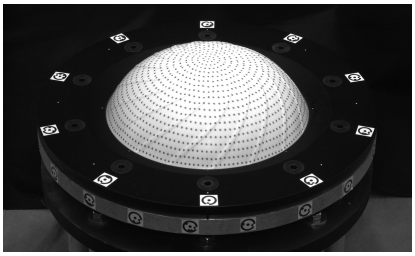

C. $t = 140$ s

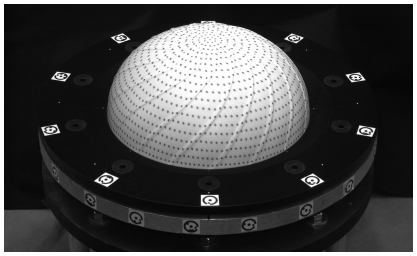

D. $t = 210$ s

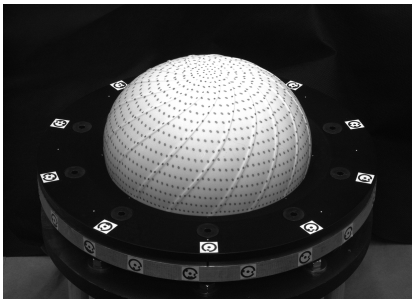

E. $t = 280$ s

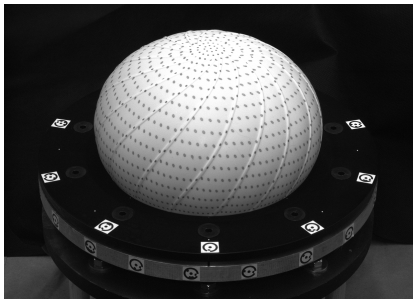

F. $t = 424$ s

Figure 3.52: Photographs of the spirally reinforced membrane at selected times during inflation.

Figures 3.52C–3.52F show snapshots of the membrane at four instants of time during inflation.

By looking at the snapshots of the deformation, we can see that the inflation of the membrane combines three motions; vertical translation, radial expansion, and twist. The twist in this case is a natural effect that occurs to optimize the energetic tradeoffs between fiber elongation and matrix distortion [96]. As a result, the initially curved fibers in the undeformed configuration will tend to straighten out as the inflation proceeds. This will lead to inflation-induced deformations with a high degree of localized shearing and significant overall twisting. The amount of twist at the crown of the membrane can be measured using photogrammetry. Figure 3.53, shows the amount of rotation of the crown (Φ_{0z}) about the vertical axis, during inflation. As can be seen, within the inflation range of this experiment, the twist amount almost linearly increases as the pressure goes up. Although not shown here, the amount of twist is expected to reach an asymptote as the pressure gets higher.

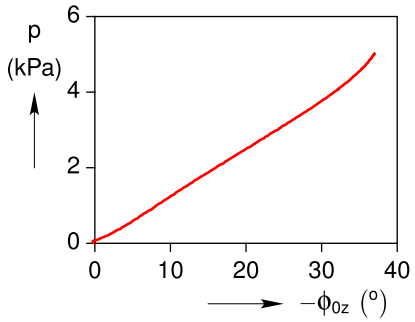

Figure 3.53: Rotation of the crown during inflation of the spiral bimaterial membrane.

The pressure and volume-change histories during inflation are demonstrated in Figures 3.54A and 3.54B. The pressure-volume cross plot is shown in Figure 3.54C.

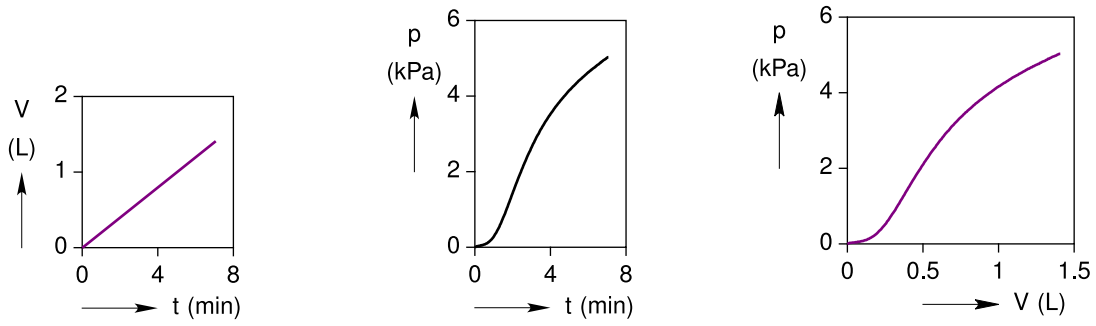

A. Volume history B. Pressure history C. Pressure-volume

Figure 3.54: Structural response of the spiral bimaterial membrane.

Figure 3.55 provides information about the membranes response near the crown. In particular, the pressure-stretch data is shown in Figure 3.55A. Because of the rotational symmetry, the two principal stretches are equal at the crown. The membrane starts from an undeformed state (λ_0 =1) and reaches to a stretch ratio of near λ_0 =1.2 at about p =5.0 kPa. Moreover, it can be seen from Figure 3.55B that the two principal curvatures are (almost) identical, and on average, demonstrate a similar trend to the axisymmetric cases. The jaggedness in the curvature response is associated to the fact that some of the dots that were used to calculate the curvatures, were located at the boundary of the (stiff) fiber and (soft) matrix, resulting in non-smooth measurements.

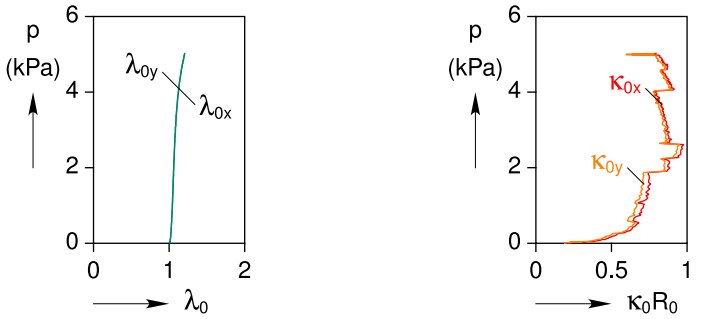

A. pressure-stretch B. pressure-curvature

Figure 3.55: Measured data at the center of the spiral bimaterial membrane.

The variation of the radial and hoop stretch ratios, λ_R and λ_Θ, are plotted at the time of maximum inflation as a function of dimensionless radius (R/R_0) of the undeformed configurations in Figure 3.56. As can be seen, the variations of both λ_R and λ_Θ along the radius, are quite jagged. The reason is that a radial line that extends from the center towards the edge, crosses the spiral fibers at multiple locations, and the discontinuity in the stiffness of the matrix and fiber, results in such a jagged behavior. More specifically, the valleys of the λ_R and λ_Θ plots correspond to the locations of the fibers along the radius, which get less stretched compared to their neighboring matrix because of their higher stiffness ans aspect ratio.

The dimensionless deformation profile history of the inflated membrane at selected instants of time are depicted in Figures 3.57A and 3.57B in two planes cutting through the membrane, namely the X-Z and Y-Z planes. In addition to the deformation profiles, the position history of the black dots during the inflation processes, are demonstrated in these plots. As can be seen the deformation is rotationally symmetric.

Variations of the invariants of the left Cauchy-Green deformation tensor ($\boldsymbol{B}$) across the surface of the membrane are studied next. Figure 3.51 present the 3D contour plots of the quantities $I_1 - 3$ and $I_2 - 3$ on the deformed configuration at different time frames.

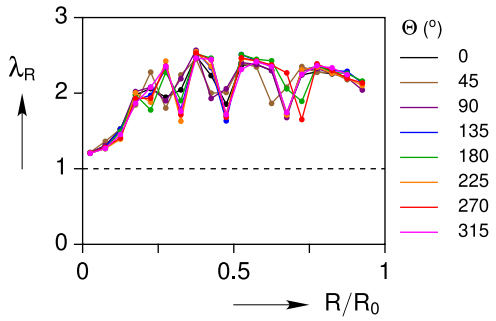

A. Radial stretch profiles

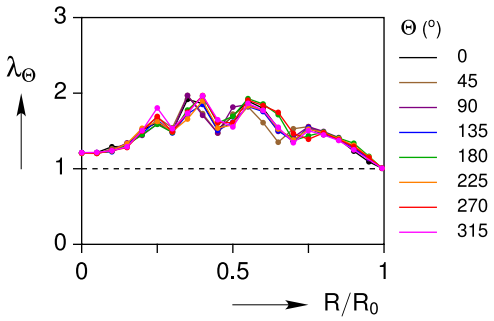

B. Hoop stretch profiles

Figure 3.56: Radial distributions of the stretch ratios in the spiral bimaterial membrane at the time of maximum inflation.

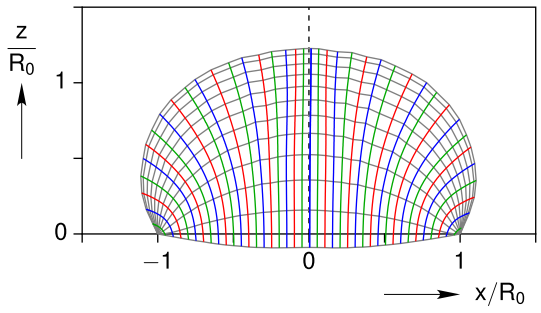

A. $Y = 0$ plane

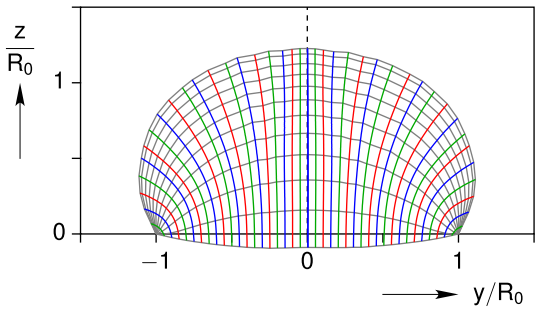

B. $X = 0$ plane

Figure 3.57: Measured deformation profiles (gray lines) and displacement histories of dots (colored lines) during inflation of the spiral bimaterial membrane.

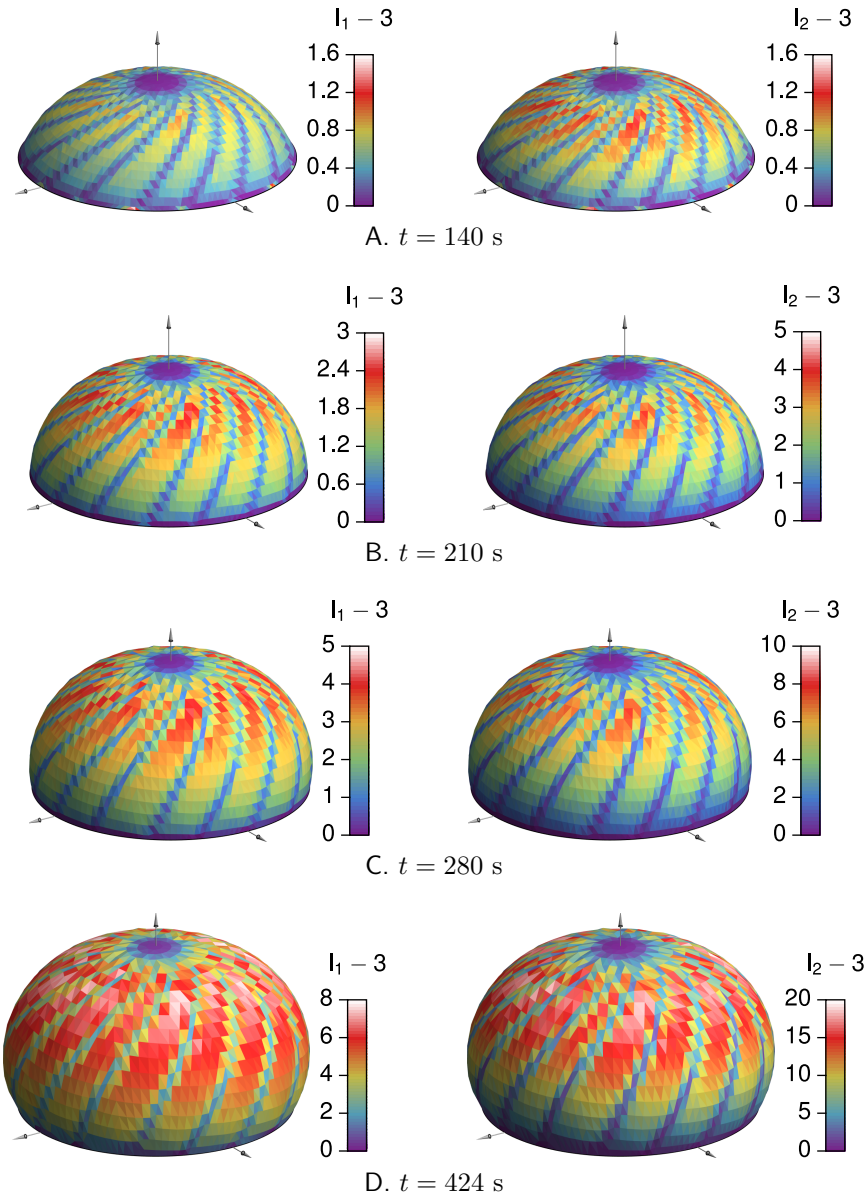

Figure 3.58: Measured contours of $I_1(\boldsymbol{B})$ and $I_2(\boldsymbol{B})$ for the spiral bimaterial membrane.

3.6 Conclusions

We presented the response of shape morphing architectured deformable solids in the context of inflatable membranes. We demonstrated a few examples of feasible shapes that can be achieved upon inflation of initially flat circular rubber membranes. The main contributions of this study were the implementation of geometrical and material nonuniformities to achieve nontraditional shapes and motions from the pressurization of simple circular membranes. The case studies included the axisymmetric inflation of membranes with linearly varying thicknesses as well as non-axisymmetric inflation of an diametrically varying thickness, a bimaterial uniform thickness, and a spirally reinforced uniform thickness membrane. We showed that it is possible to achieve negative curvatures and twist during pressurization by selectively changing the distribution of materials in the membrane.

The photogrammetry technique using nine cameras was used to obtain the 3D displacement field for each study. The 3D data of black dots on the membrane was used to reconstruct the 3D surface of the membrane and analyze the variation of field quantities across the membrane. Several numerical finite-element simulations were performed to assist with the parametric study on the effect of thickness distribution on the response, deformation, and stability of axisymmetric membranes. Our rubber-based prototypes provide a convenient basis for conceptual scientific and design explorations in shape morphing inflatable structures.

CHAPTER 4

A Biomimetic Robotic Jellyfish Based on Shape Memory Alloy Springs

4.1 Introduction

The development of robotic underwater vehicles has grown continuously in recent decades thanks to the potential applications of these systems and advancements made in the sensors and actuation devices. These robots have been utilized in numerous applications, including water sampling, underwater ecological change monitoring, oil and gas explorations, and hydrographic surveys [97, 98]. Compared to the traditional methods of underwater sensing with human-operated submarines, underwater robots offer potential benefits in cost-effectiveness, compactness, range of operation, and extended lifetime. Since animal locomotion in nature tends to use the optimal motion for its living environment, biomimetic robots have become a particular research focus. In early underwater robots, locomotion was accomplished by traditional piston and motor actuators, usually involving complex linkage mechanisms. Despite improvements in later attempts, the size and weight were still critical issues and the life-time was limited because of the excessive number of parts (see the review in [99]).

Jellyfish are among the simplest animals, containing only a few organs, with axisymmetric bodies. Jellyfish are known to be one of the most efficient ocean swimmers, spending less energy per distance than many other underwater creatures. This is accomplished by recapturing part of the expended energy of each stroke [100]. Jellyfish are classified in the subphylum Medusozoa, which comprises a major part of the phylum Cnidaria. Of the swimming Medusozoa found in nature, the two main classes are Scyphozoa (*true jellyfish*) and Cubozoa (*box jellyfish*). Both have hemi-ellipsoidal bells, but as shown in Figure 4.1, the Scyphozoa's is *oblate* (saucer-like) whereas the Cubozoa's is *prolate* (bullet-like). True jellyfish swim through a combination of rowing and jet propulsion, whereas box jellyfish swim using jet propulsion only [101, 102]. In jet propulsion, water is squeezed out of the bell

periodically to produce the required thrust. By contrast, rowing propulsion uses the weak subumbrellar muscles to row at the bell periphery to form vortex rings in the water [103]. True jellyfish generally swim quite slowly, while box jellyfish swim somewhat faster through a darting motion. The slow motion of the true jellyfish inspired us to mimic its locomotion through the use of shape memory alloys (SMAs) as artificial muscles.

Our objective is to demonstrate a simple, compact, and biomimetic soft underwater robot using smart materials. Soft robots, as opposed to conventional robots, may be more environment-friendly as they reduce the unintended harm to the aquatic ecosystem of underwater vegetation and marine animals [104]. Among the known smart materials, NiTi-based SMAs provide some of the highest energy densities available, with typical transformation strains near 5% at actuation stresses of 200 MPa or more. In addition, NiTi-based SMAs are corrosion-resistant, biocompatible, and have ultimate tensile strengths above 1 GPa. A well known disadvantage of SMAs, however, is the slow actuation compared to other smart materials or conventional actuators. The response time of SMAs is dictated by heat-transfer considerations; in an actuation mode, the response time is most often limited by the cooling segment. An underwater environment, however, improves the cooling rate of the SMA and enables useful actuation cycle rates.

Similar past efforts include the following. Yang *et al.* [105] developed a jellyfish microrobot of a hemispherical body shape made of a rubber material that incorporated a circumferential SMA actuator and four ionic polymer–metal composite (IPMC) legs for swimming. The proposed design achieved a maximum speed of 6 mm/s at an operating frequency of 0.6 Hz. Villanueva *et al.* [106] designed a robotic jellyfish that incorporated a beam-shape composite actuator based on SMA wires as the active component of the muscle. The design was inspired by contraction of a jellyfish bell through a combination of rowing and jetting mechanisms for locomotion [107] and reached a maximum speed of 54 mm/s at 0.5 Hz. Also, Gao *et al.* [108] fabricated a biomimetic cuttlefish robot that swam at relatively high speed (87.6 mm/s) through a jetting propulsion mechanism. The propulsion was achieved by squeezing water out of the mantle cavity by heating of SMA wires embedded in a soft silica gel. Their design achieved a maximum average jet thrust of 0.14 N at a jetting frequency of 0.83 Hz. Furthermore, Kim *et al.* [109] developed a turtle-like swimming robot where propulsion was achieved through flapping motion of two soft actuators made using SMA wires that served as the turtle's flippers and could generate bending and twisting motions. The robot was able to reach a swimming speed of 22.5 mm/s.

Our ongoing work explores an alternative SMA actuation approach to create a simple, compact, high-performance, biomimetic jellyfish, with initial results first reported in [43]. The main contribution is the simplicity of design, requiring only a soft rubber matrix with a

A. Scyphozoa (True jellyfish) [110]

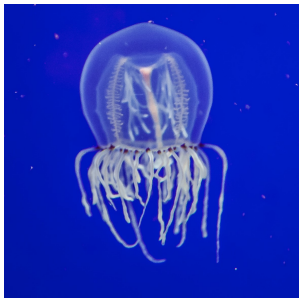

B. Cubozoa (Box jellyfish) [111]

Figure 4.1: Photographs of the two main classes of swimming jellyfish

single embedded SMA spring acting as the artificial muscle. Large deformations are achieved without the need for extra mechanical parts and joints, actuation cycles are demonstrated at comparable rates to previous attempts (0.5 Hz), and the robot swims with a motion reminiscent of the actual jellyfish.

The chapter begins with an overview of the proposed robot design, materials, and fabrication method. A nonlinear finite-element simulation demonstrates the buckling behavior of the robot structure. The typical swimming performance of our prototype is reviewed, followed by an experimental parameter study of the sensitivities of important operational and design parameters, including new results beyond those in [43].

4.2 The robot jellyfish

4.2.1 Design & operation

We chose to mimic the true jellyfish of the oblate form (Figure 4.1A), which uses the hybrid rowing and jetting modes for propulsion. The robot design is a flat rubber slab (h = 3.8 mm thick) in a sunburst shape, consisting of a central circular (D = 76 mm nominal diameter) disk with up to eight radially protruding flaps (see Figure 4.4A). The tip-to-tip diameter across the flaps is about 140 mm. An SMA tension spring, embedded near the periphery of the central disk in a circular loop, serves as the circumferential muscle of the robot (Figure 4.4F). The alloy is chosen to have a characteristic transformation temperature well above room temperature, so the SMA phase is martensite at room temperature and austenite when sufficiently hot. The SMA spring is pre-stretched at room temperature such that the phase is oriented martensite and is cast in place within the rubber. The SMA spring is heated by running electrical current through two lead wires attached to the ends of the

spring loop. The shape memory effect causes the spring to transform to the much stiffer austenite and contract in length, which creates a radial inward pressure to buckle the rubber disk into a dome shape. The flaps then follow the rotation of the disk edge, causing them to paddle downward and inward towards the axis of the dome.

The SMA spring cools back to the ambient temperature and reverts to the more compliant martensite phase, once the electric current is turned off. The spring is sized such that the rubber matrix has sufficient stiffness to return the structure toward its prebuckled, flat configuration. The locomotion of the robot results from the abrupt buckling of the disk that creates a propulsive jet along with the downward rowing of the flaps, followed by a relatively slow reset to the flatter configuration in order to minimize the opposing drag in the water. Each actuation cycle produces a net translation upward, and the robot is kept swimming by repeating the cycle.

4.2.2 Material behavior

4.2.2.1 SMA material

The synthetic jellyfish structure consists of two components, an SMA spring loop and an elastomeric matrix. Close-coiled SMA tension springs ($d_s^o = 2.5$ mm outer diameter), made from $d_w = 0.38$ mm diameter 90C Flexinol® wire, were purchased from Dynalloy Inc. The spring index was $c = d_s/d_w = 5.67$, based on the nominal spring diameter $d_s = d_s^o - d_w$. The uniaxial thermo-electro-mechanical response of this wire was characterized previously in [112] and the results of a differential scanning calorimetry (DSC) test are reproduced here in Figure 4.2. It shows the input heat rate (normalized by the temperature rate) to a small stress-free sample of 90C Flexinol wire during a prescribed heating and cooling temperature scan. The baseline specific heat is about $c_0 = 0.5$ J/(g-K) for sensible heating and the shaded area under the peak at 77 °C shows the (endothermic) latent heat of transformation from martensite to austenite ($\Delta H_{AM} = 21$ J/g). During cooling, the valley at 50 °C shows the exothermic latent heat of transformation from austenite to martensite. Thus, under stress-free conditions at temperatures below the martensite finish temperatures near $M_f = 40$ °Cthe material is thermal martensite, while above the austenite finish temperatures near $A_f = 85$ °C the material is austenite. In between these temperatures, the phase of the material depends on the prior temperature history and may be a mixture of austenite and martensite. With the application of mechanical stress, these transformation temperatures shift to higher temperatures, consistent with the well-known Clausius-Clapeyron law.

The elastomeric matrix is made from the two-part Ecoflex 00-30 platinum-catalyzed silicone rubber from Smooth-On Inc. The as-cured rubber has a Shore hardness of 00-30

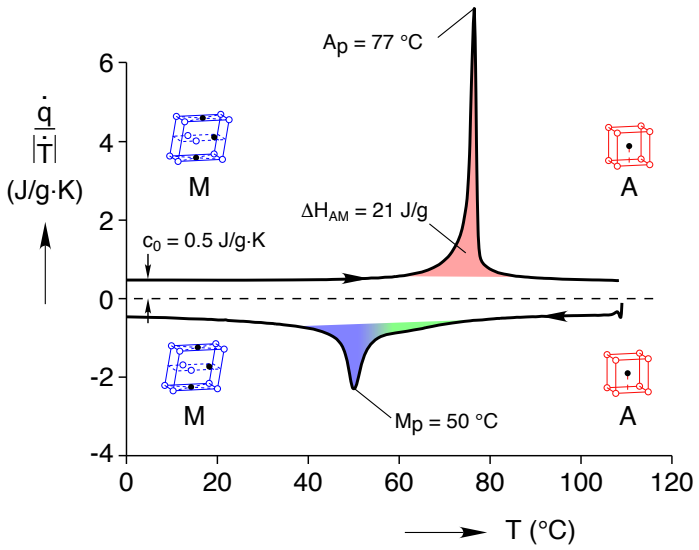

Figure 4.2: Differential Scanning Calorimetry (DSC) thermogram of 90C Flexinol (after [112]).

and a mass density of $\rho = 1070$ kg/m^3, as indicated by the supplier. The silicone rubber is quite compliant, similar to a soft gel shoe insert, and can withstand large deformations without permanent damage.

4.2.2.2 Silicone rubber material

The jellyfish body was mainly composed of the two-part Ecoflex 00-30 platinum-catalyzed silicone rubber, which was purchased from Smooth-On Inc. and used as received. As specified by the supplier, the as-cured rubber has a density of $\rho = 1070$ kg/m^3 and a Shore hardness of 00-30. The mechanical behavior of this silicone rubber is quite soft, similar to the soft gel insole used in a shoe for example. It can withstand large deformations without permanent damage, and its mechanical response has little hysteresis. This means the mechanical behavior of the jellyfish body can be analyzed in the context of finite elasticity with a hyperelastic constitutive model. Consistent with the usual approach for analyzing elastomeric structures, we considered the constitutive response of silicone rubber to be isotropic, incompressible, and nonlinearly elastic.

For its simplicity, we chose the Mooney-Rivlin hyperelastic model (Table 3.1) with a strain energy density function $\widehat{W}$ of the form

$$\widehat{W}(I_1, I_2) = c_1 (I_1 - 3) + c_2 (I_2 - 3) . \tag{4.1}$$

Table 4.1: Mooney-Rivlin stresses for the three constitutive tests.

Uniaxial Tension	**Planar Tension**	**Equi-biaxial Tension**
$\sigma = 2\left(c_1 + c_2\lambda^{-1}\right)\left(\lambda^2 - \lambda^{-1}\right)$	$\sigma = 2\left(c_1 + c_2\right)\left(\lambda^2 - \lambda^{-2}\right)$	$\sigma = 2\left(c_1 + c_2\lambda^2\right)\left(\lambda^2 - \lambda^{-4}\right)$

In the small strain limit, the Mooney-Rivlin model gives a shear modulus of $\mu_0 = 2(c_1 + c_2)$, which effectively imposes a constraint on the two material parameters to give a stable shear response ($\mu_0 > 0$). Although the Mooney-Rivlin model shows good agreement with tensile test data of typical elastomeric materials in the small to moderate stretch range (say $\lambda < 2$), it fails to account for the hardening of the material at large stretches, in which case a different hyperelastic model would be needed. Fortunately, the finite-element simulation of the jellyfish in the next section confirms that the local stretch ratios are moderate, so the Mooney-Rivlin model is sufficient for our purposes.

Table 4.1 summarizes the Cauchy stress-stretch relations for each of the constitutive tests, defined in Section 3.2, with the Mooney-Rivlin model.

The material parameters of the Mooney-Rivlin model were obtained by a simultaneous nonlinear least squares fit of data from the three constitutive tests. Since experimental measurements were performed with respect to their reference (initial) dimensions, the Cauchy stresses in Table 4.1 were converted to engineering (nominal) stresses by $\sigma_{\text{eng}} = \sigma/\lambda$. The fitted curves of the Mooney-Rivlin model to the stress-stretch responses of the constitutive experiments are shown in Figure 4.3. The material parameters were found to be $c_1 = 13$ kPa and $c_2 = 1.4$ kPa, for the batch of the silicone rubber used in this experiment. These values are used in the upcoming finite-element simulation.

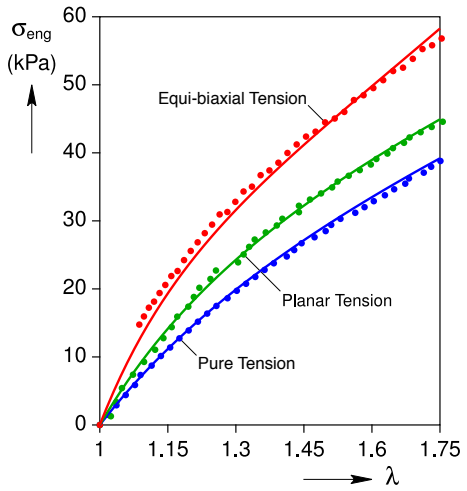

Figure 4.3: Mechanical characterization of silicone rubber: experimental data (dots) and Mooney-Rivlin fit (solid lines).

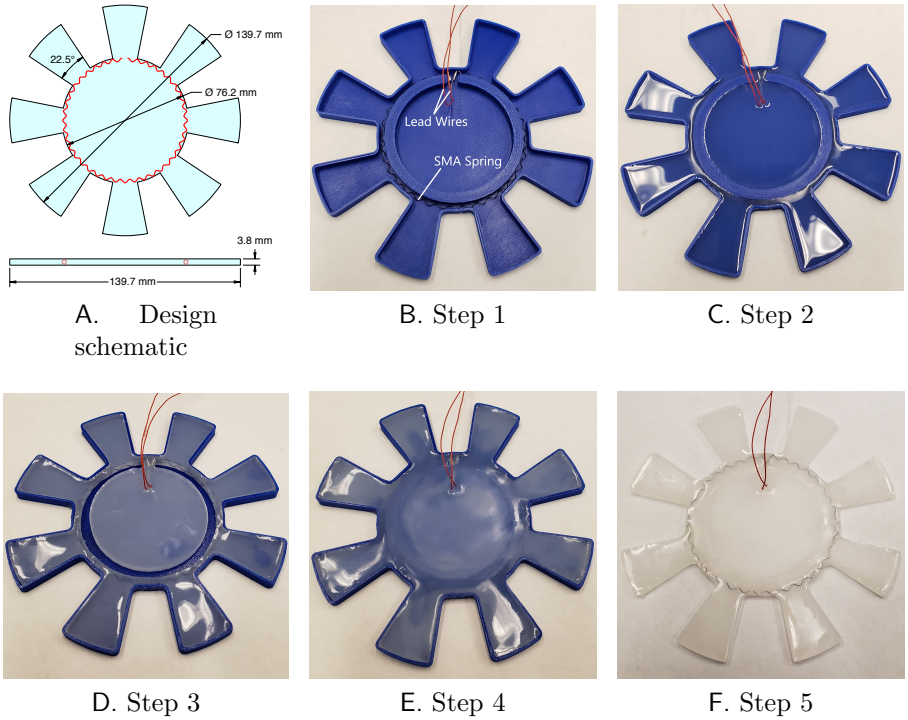

A. Design schematic B. Step 1 C. Step 2

D. Step 3 E. Step 4 F. Step 5

Figure 4.4: Jellyfish robot design (A) and fabrication procedure (B–F): (B) the SMA spring loop and lead wires are placed in the primary mold; (C) liquid silicone rubber is poured in the primary mold; (D) after curing, the incomplete robot is removed and placed in the secondary mold; (E) additional rubber is poured to complete the robot body; (F) after curing, the completed robot jellyfish is removed.

4.2.3 Fabrication

The body of the prototype robot jellyfish is fabricated from silicone rubber using custom-made molds as described in [43]. Two molds were designed and 3D printed, and the body of the jellyfish was cast in a few steps. We found it important to precisely place the SMA spring loop in a concentric initial configuration, so the primary mold has a raised ring to provide a circular slot (73.7 mm inner diameter, 2.5 mm width) to hold it in place during casting. It also includes a radial slot to allow electrical lead wires to be attached to the spring loop and led radially toward the disk's center. The secondary mold had the same outer envelope as the primary mold, but without the raised ring, and it was used to complete the casting of the center disk of the jellyfish body.

About 38 coils of the SMA spring were excised, and the spring sample was heated above the austenite finish temperature until a nearly close-coiled spring was obtained ($L_0 = 27$ mm reference length). The SMA spring was then pre-stretched to fit the circumferential length of the primary mold's slot, giving a pre-stretch of about $\lambda_0 = L/L_0 \approx 16$ in the baseline case. At each end of the SMA spring, a short length of the SMA wire was straightened,

crimped with a ferrule, and soldered to 30-gauge lead wires. This assembly was then placed in the primary mold (Figure 4.4B).

After weighing and degassing, liquid Ecoflex 00-30 silicone rubber was poured over the SMA spring within the outer region of the primary mold (Figure 4.4C) and then allowed to cure for at least 4 hours at room temperature. After curing, the incomplete jellyfish was removed from the primary mold and placed into the secondary mold (Figure 4.4D). Additional liquid rubber was then poured into the remaining central hole in the jellyfish body and cured for another 4 hours (Figure 4.4E). The jellyfish was removed from the mold and longer lead wires were soldered to the leads exiting the jellyfish body so that it could be connected to a power supply. Excluding lead wires, the entire robot jellyfish mass is about 40 g (Figure 4.4F).

4.3 Analysis & simulation

Our purpose here is to establish a simple scaling law for the actuation of the jellyfish and then to present a finite-element simulation of the jellyfish post-buckling deformation. The contraction of the circumferential SMA spring loop is intended to create an inward radial pressure and to buckle the central disk region of the jellyfish body (Figure 4.5A). The buckling analysis of a circular plate under uniform radial compression pressure on its edge has been studied extensively [113, 114, 115, 116], and the critical pressures have been investigated for different supporting boundary conditions and buckling mode shapes. The present analysis extends this boundary value problem (BVP) to account for the inelastic pre-stretch and the elastic stretch of an actuated SMA spring as a result of heating. For simplicity of analysis, the rubber circular plate is treated as an isotropic linear elastic material, and the SMA spring is treated as a one-dimensional homogenized element. To justify the linear elastic assumption in the rubber it will be verified that the onset of buckling in the rubber disk occurs at small strains. The post-buckling analysis, however, will require a fully nonlinear solution, which will be accomplished by the numerical finite-element analysis that follows.

Before the composite buckling problem is presented, the buckling analysis of a linear elastic disk under radial pressure is reviewed. A circular flat plate of initial radius a_0 and thickness h_0 consists of a material with elastic modulus E and Poisson's ratio ν and is subject to a uniform radial compressive pressure p (Figure 4.5B). The Von Karman plate equation written in polar coordinates for the transverse deflection $w(r,\theta)$ [117] is

$$D_m\left(\frac{\partial^2}{\partial r^2}+\frac{1}{r}\frac{\partial}{\partial r}+\frac{1}{r^2}\frac{\partial^2}{\partial \theta^2}\right)\left(\frac{\partial^2 w}{\partial r^2}+\frac{1}{r}\frac{\partial w}{\partial r}+\frac{1}{r^2}\frac{\partial^2 w}{\partial \theta^2}\right)-N^0_{rr}\frac{\partial^2 w}{\partial r^2}-N^0_{\theta\theta}\left(\frac{1}{r}\frac{\partial w}{\partial r}+\frac{1}{r^2}\frac{\partial^2 w}{\partial \theta^2}\right)=0, \tag{4.2}$$

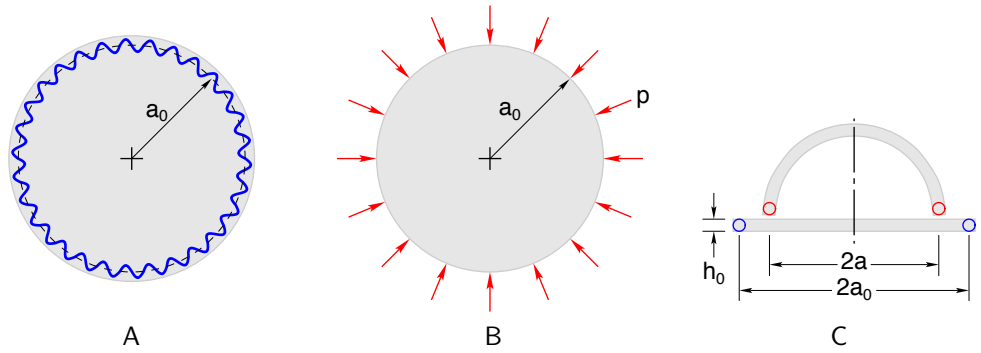

Figure 4.5: Schematics of the BVP analyzed: (A) rubber disk with embedded SMA spring, (B) flat disk subject to uniform radial pressure, (C) cross-section of reference and buckled configurations.

where N^0_{rr} and $N^0_{\theta\theta}$ are the prebuckled stress resultant intensities, and the flexural rigidity of the plate is

$$D_m = \frac{E\, h_0^3}{12\,(1-\nu^2)}. \tag{4.3}$$

Since the prebuckled problem is axisymmetric, the load intensities are $N^0_{rr} = N^0_{\theta\theta} = -h_0 p$. If only the axisymmetric instability modes are sought such that $w = w(r)$, the equilibrium equation Equation (4.2) simplifies to

$$D_m\left(\frac{\partial^4 w}{\partial r^4} + \frac{2}{r}\frac{\partial^3 w}{\partial r^3} - \frac{1}{r^2}\frac{\partial^2 w}{\partial r^2} + \frac{1}{r^3}\frac{\partial w}{\partial r}\right) + h_0 p\left(\frac{\partial^2 w}{\partial r^2} + \frac{1}{r}\frac{\partial w}{\partial r}\right) = 0. \tag{4.4}$$

The analysis is further simplified by introducing the dimensionless parameters

$$k = a_0\sqrt{\frac{h_0 p}{D_m}}, \quad \bar{r} = \frac{r}{a_0}, \quad \bar{w} = \frac{w}{a_0}, \quad \bar{h} = \frac{h_0}{a_0}. \tag{4.5}$$

The general solution to Equation (4.4) for the dimensionless transverse displacement $\bar{w}$ is

$$\bar{w}(\bar{r}) = c_1 \ln(\bar{r}) + \frac{c_2}{k^2}\left[1 - J_0(k\bar{r})\right] - \frac{c_3}{k^2} Y_0(k\bar{r}) + c_4, \tag{4.6}$$

where $\{c_1, c_2, c_3, c_4\}$ are constants and $J_n(x)$ and $Y_n(x)$ are Bessel functions of first and second kind, respectively. A finite deflection at the center of the plate ($r = 0$) requires that $c_1 = c_3 = 0$. For a simply supported plate edge, the zero deflection and zero moment

boundary conditions become

$$\bar{w}(1) = 0, \quad \frac{\partial^2 \bar{w}(1)}{\partial \bar{r}^2} + \nu \frac{\partial \bar{w}(1)}{\partial \bar{r}} = 0. \tag{4.7}$$

Substituting Equation (4.6) along with $c_1 = c_3 = 0$ into Equation (4.7) gives a homogeneous system of linear equations, for which non-trivial solutions are possible if the following characteristic equation is satisfied

$$kJ_0(k) - (1-\nu)J_1(k) = 0. \tag{4.8}$$

Assuming the disk material is incompressible ($\nu = 1/2$), the critical compressive load is obtained by solving Equation (4.8) for the smallest positive root k, which is found numerically as

$$k_c = 2.16587. \tag{4.9}$$

Using Equations (4.3), (4.5) and (4.9) with $\nu = 1/2$, the critical buckling pressure p_c can be found from

$$\overline{p}_c \equiv \frac{p_c}{E} = \left(\frac{k_c \bar{h}}{3}\right)^2. \tag{4.10}$$

Based on the dimensions described in Sections 4.2.1 and 4.2.3 and assuming the mean radius of the disk in Figure 4.5A and its elastic modulus (in small strain limit) to be $a_0 = 38.1 - 1.3 = 36.8$ mm and $E = 3\mu = 86.4$ kPa, respectively, the critical buckling pressure is calculated to be $p_c = 0.48$ kPa. Using Equation (4.10), the non-dimensionalized critical buckling pressure is $\overline{p}_c = 0.0052$, accordingly, which is equivalent to a critical buckling strain of $\varepsilon_c = -p_c/(2E) = -0.0028$ in the rubber disk. Thus, the small strain assumption in the rubber is verified, at least at the onset of buckling.

Considering now the SMA spring loop, equilibrium and compatibility with the rubber disk are enforced as follows. The SMA loop is assumed to have a reference length $L_0 = 2\pi b_0$ corresponding to a loop radius of b_0 in the load-free hot austenite phase. The SMA is cooled down to room temperature, the martensite spring is stretched to a larger loop radius of a_0, and then the spring is installed in the rubber as it cures. This defines the pre-stretch ratio $\lambda_0 = a_0/b_0$, where the SMA spring has an inelastic strain and both the rubber and the SMA are stress-free. Upon heating to austenite, the SMA spring attempts to contract to its reference length L_0 but is impeded by the opposing radial outward pressure p from the elasticity of the rubber disk inside the spring loop. The 'tug-of-war' between the SMA

spring and the rubber results in a current loop radius of a, somewhere in between b_0 and a_0. Considering equilibrium of the free body diagram in Figure 4.6, the tension in the SMA spring is

$$F = ah_0p. \tag{4.11}$$

At this point we require a relation between the radius a and the tension in the spring F. Fortunately, the 'constitutive' law for the hot SMA spring is simple. It is just a linear force-elongation law based on the initial length $2\pi b_0$ and the current length $2\pi a$ in terms of the effective spring stiffness K_{A} in the austenite phase,

$$F = 2\pi K_{\mathrm{A}} \left(a - b_0\right). \tag{4.12}$$

Equating Equation (4.11) and Equation (4.12) gives the pressure-radius relation

$$p = 2\pi \frac{K_{\mathrm{A}}}{h_0} \left(1 - \frac{b_0}{a}\right). \tag{4.13}$$

The current radius a must be compatible with the hoop strain in the rubber $\varepsilon_\theta = a/a_0 - 1$, so eliminating a in Equation (4.13) and linearizing with respect to ε leads to

$$p = 2\pi \frac{K_{\mathrm{A}}}{h_0} \left[1 - \frac{1}{(1+\varepsilon)\lambda_0}\right] \approx 2\pi \frac{K_{\mathrm{A}}}{h_0} \left[1 - \frac{1-\varepsilon}{\lambda_0}\right]. \tag{4.14}$$

Substituting the constitutive relation $\varepsilon = -p/(2E)$ and solving for p, gives the pressure in terms of geometric and material parameters and the pre-stretch ratio,

$$\frac{p}{E} = 2\frac{\lambda_0 - 1}{1 + \overline{E}\lambda_0}, \quad \text{with } \overline{E} \equiv \frac{Eh_0}{\pi K_{\mathrm{A}}}. \tag{4.15}$$

This pressure must be sufficient to buckle the rubber disk ($p > p_{\mathrm{c}}$), so Equation (4.10) requires a minimum pre-stretch of

$$\lambda_0 > \lambda_0^{\mathrm{c}} \equiv \frac{2 + \overline{p}_{\mathrm{c}}}{2 - \overline{p}_{\mathrm{c}}\overline{E}}. \tag{4.16}$$

In addition, since the pre-buckled strains in the rubber are quite small, Equation (4.11) with $a \approx a_0$ can be used to estimate the tension in the spring (about $F_{\mathrm{c}} = 65$ mN) at the critical buckling pressure.

To study the post-buckling behavior, an FEA in COMSOL was performed to explore the fully nonlinear displacement and strain fields. The geometry of the entire robot jellyfish in its

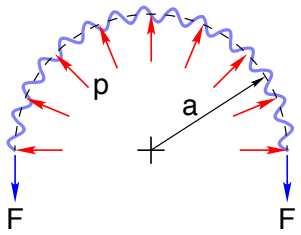

Figure 4.6: Tension in the SMA spring loop.

flat reference configuration was modeled (Figure 4.7A), and a structured mesh was defined with a finer mesh near the periphery of the center disk (Figure 4.7B). For simplicity, the SMA spring was modeled as a slender ring inclusion, with a cross-sectional area of the SMA wire and an elastic modulus much larger than that of the surrounding rubber. Contraction of the SMA element was simulated by prescribing a negative inelastic hoop strain (eigenstrain) β in the inclusion. This inelastic strain served as the loading parameter throughout the analysis. A zero axial (vertical) displacement $w = 0$ was imposed along the periphery of the inner disk. The inner disk was given a very small (1 Pa) lateral pressure as a loading imperfection to aid numerical convergence at the onset of buckling.

The 3-D deformed configurations at different stages during simulation are shown in Figures 4.7C–4.7E with contours of the normalized axial displacement, $\overline{w}$. The response of the structure during the entire simulation is shown in Figure 4.7F in terms of the normalized axial displacement of the disk center $\overline{w}(0)$ and the hoop strain inside the rubber disk at the interface with the inclusion $\varepsilon_\theta(a_0)$. The filled circle in Figure 4.7F identifies the end of the simulation, which corresponds to the deformed configuration in Figure 4.7E. The inset in Figure 4.7F provides a magnified view of the response near the onset of buckling, where the dashed line depicts the critical buckling strain ($\varepsilon_c = -0.28$ %) calculated previously. The knee in the FEA response (solid line) agrees nicely with this value.

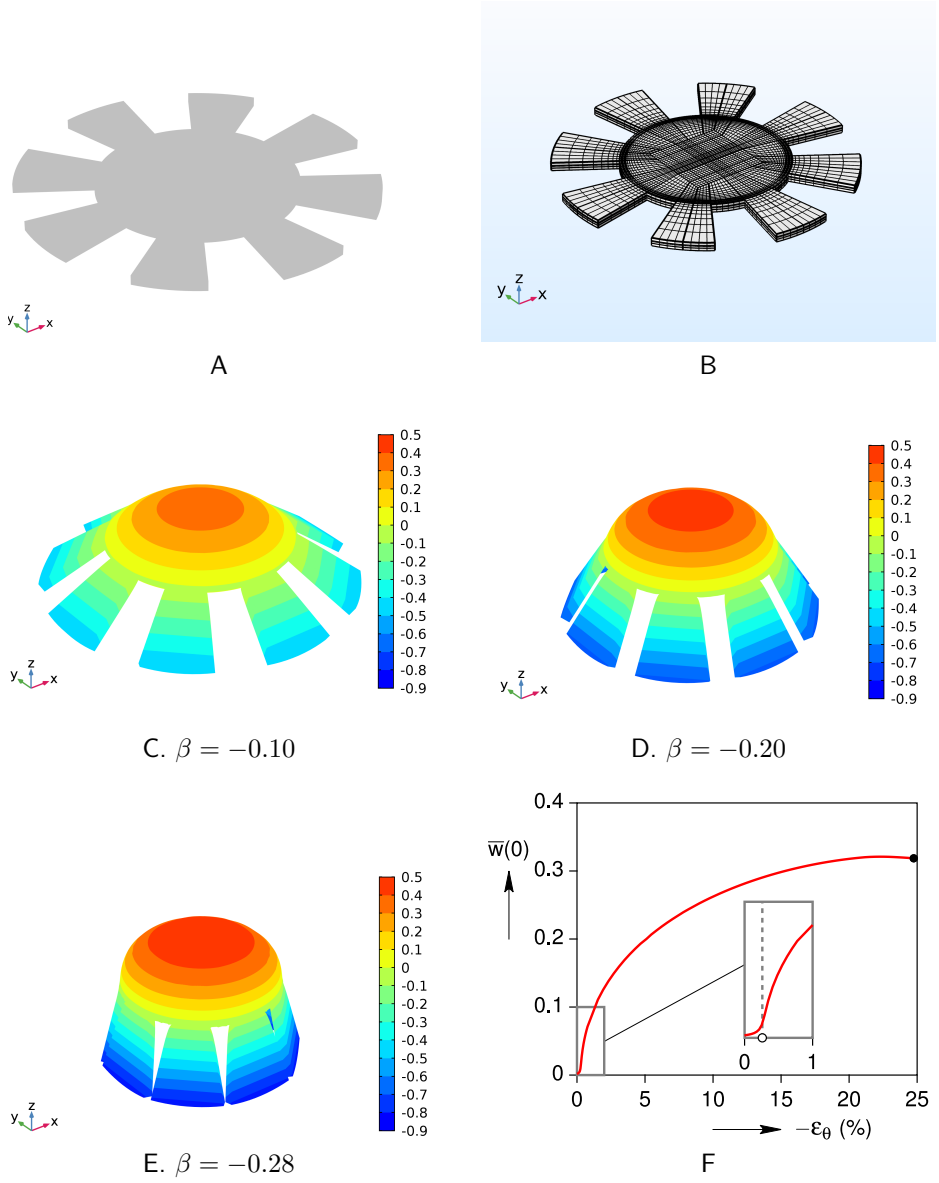

Figure 4.7: Finite-element simulation results of the robot jellyfish deformation; (A) reference geometry, (B) finite-element mesh, (C–E) contours of normalized axial displacement, and (F) response of the body during simulation with a magnified view of the response near the onset of buckling.

Further details of the deformation fields within the jellyfish body at the end of the simulation ($\beta = -0.28$) are provided in Figure 4.8. Using components of the Green-Lagrange strain tensor $\boldsymbol{\varepsilon} = (\boldsymbol{F}^\top \boldsymbol{F} - \boldsymbol{I})/2$, radial ($\varepsilon_r$) and hoop ($\varepsilon_\theta$) strain contours are shown in a section (θ=constant) of the body. Ignoring the strain concentration near the ring inclusion at the edge of the inner disk, the maximum bending strain ($\varepsilon_{r,\max} = 25.6$ %) occurs at the outer edge of the disk as indicated in Figure 4.8A. This corresponds to a radial stretch ratio of $\lambda_{r,\max} = 1.3$, confirming that the strains are comfortably within the range of accuracy of the Mooney-Rivlin model.

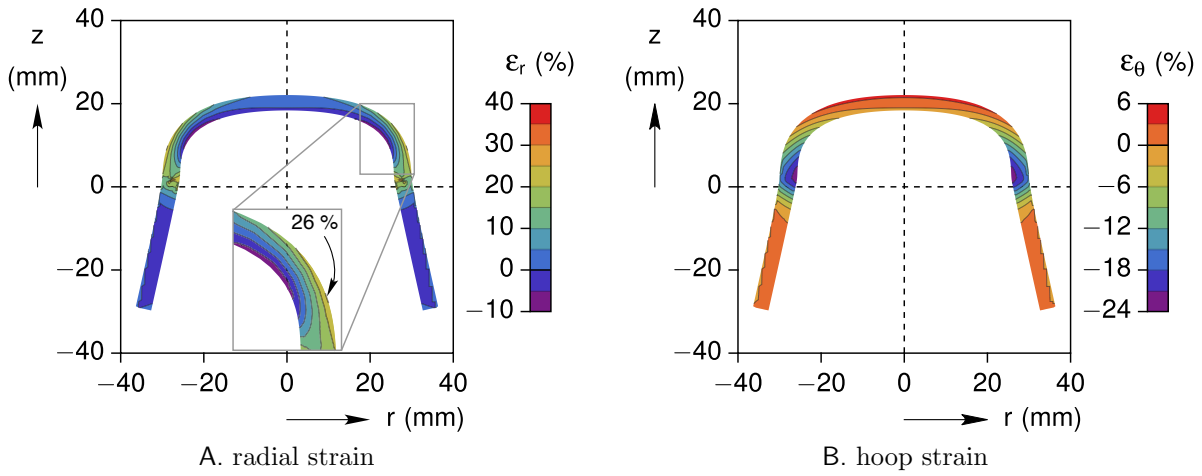

Figure 4.8: Green-Lagrange strain contours inside the deformed robot body at the end of the finite-element simulation.

4.4 Experimental results

The swimming performance of a prototype robot jellyfish is presented in this final section. Deformation and force measurements in a special static setup are also presented to quantify the underwater performance and to explore the influence of operation and design parameters, such as the input actuation power and frequency, the pre-stretch ratio of the SMA spring, and the number of flaps of the robot.

4.4.1 Swimming performance

The swimming performance of the submerged robot was evaluated based on its propulsive thrust, stroke, and the ability to reach steady-state swimming without losing performance over time. The robot had a slight negative buoyancy and was placed at the bottom of a water tank with electrical wires extending from the robot to an external power supply (see first

photograph in Figure 4.9A). Direct electrical current was applied periodically to resistively heat the SMA spring and cause it to contract within the robot.

Figure 4.9A provides a sequence of selected photographs, showing the prototype jellyfish swimming from the bottom to the top of the water tank during nine actuation cycles. The jellyfish traveled a vertical distance of about 245 mm in just over 16 s. The actuation period was 2 s (0.5 Hz actuation frequency), consisting of a constant voltage of 11.25 V (about 53.7 W) across the SMA spring for 0.25 s followed by no voltage for 1.75 s, which is equivalent to an energy consumption of about 13.4 J per cycle. A video (not shown here) of the swimming prototype showed within each actuation cycle a fast contraction followed by a slow relaxation, and the motion was reminiscent of an actual swimming jellyfish. The vertical position (z) and the upward stroke (Δz) per cycle plotted in Figure 4.9B were measured from image analysis of the photographs. As seen in Figure 4.9B, the stroke started small (under 10 mm) but the amplitude quickly grew after a few cycles to reach a nearly steady-state value of almost 40 mm/cycle by cycle 8, which corresponds to an average vertical speed of approximately 20 mm/s.

The stroke is initially small in the first few cycles, since both the rubber and SMA spring start at room temperature (cold) and the short duration of the input power is insufficient to completely transform the SMA from tensile martensite (M^+) to austenite (A). Consequently, the SMA spring only partially contracts. Upon continued cycling, however, the average temperature of the body and the spring loop increases until the temperature oscillations span the $M^+ \rightarrow A$ and $A \rightarrow M^+$ transformation temperatures during steady-state operation. That is, the SMA spring requires a few transient cycles before it warms up to an optimal mean temperature to achieve full contraction and relaxation. Subsequent actuation cycles produce larger deformations of the robot's body and larger swimming strokes.

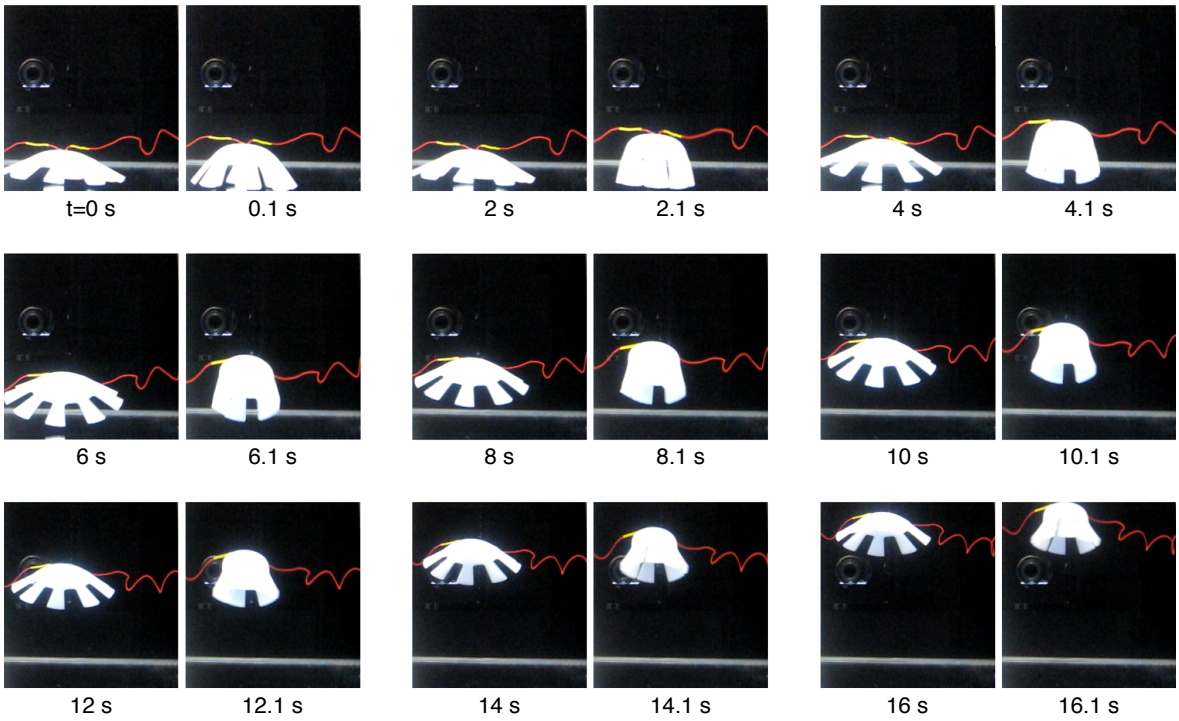

A. Photographs of swimming robot

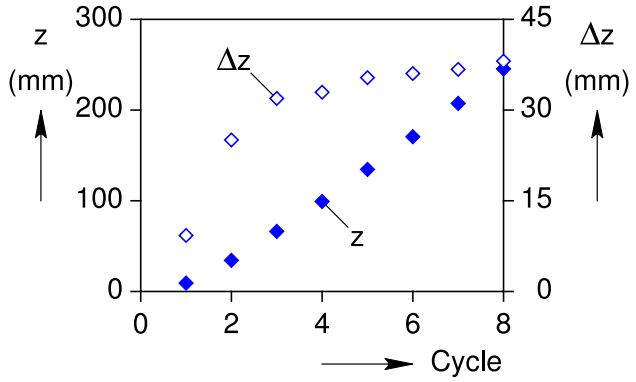

B. Vertical position and stroke

Figure 4.9: Swimming performance: (A) selected photographs of the prototype robot swimming upward (0.5 Hz actuation frequency), (B) vertical position z and stroke Δz at successive actuation cycles.

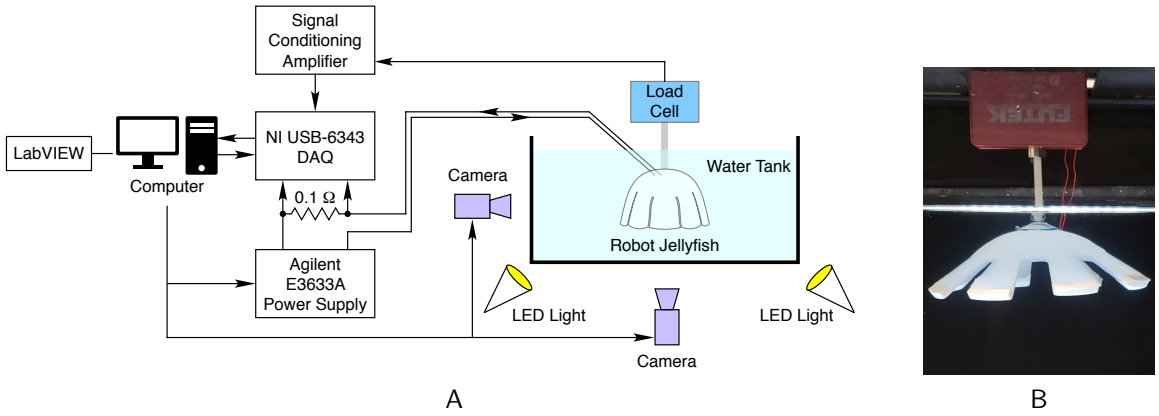

Figure 4.10: Static test setup for deformation and thrust measurements. (A) Schematic of experimental setup and (B) closeup photograph of the robot.

4.4.2 Thrust Performance

A static test rig (Figure 4.10A) was developed to quantify the thrust performance and overall deformation of the jellyfish robot. The submerged prototype jellyfish was attached by a rigid rod to a load cell (Futek LRF400, 10 N capacity) above the water tank (Figure 4.10B) to measure the thrust; synchronized images were taken by two CCD cameras to monitor the body deformation.

The submerged robot was actuated relatively fast, with approximately 12 V (about 73 W power) across the SMA spring for 0.2 s, followed by 1.8 s off for recovery, resulting an energy consumption of about 15 J in each actuation cycle. This corresponded to a total period of 2 s and a duty-cycle of 10%. From analysis of the digital images, the radial displacements of the tip of the flaps were measured (u_f) and then normalized by the initial flap tip radius (R_f = 69.2 mm, the outer envelope of the entire robot) to obtain a strain-like measure ($\overline{u}_f = u_f/R_f$) of the overall body deformation. The time history of this normalized flap displacement over several cycles is shown in Figure 4.11A, exhibiting contractions of near 60% after a few cycles. The gray line in Figure 4.11A depicts the average flap displacement during each cycle, and the unfilled circles indicate the deflection at the end of each cycle. While the prototype reached an almost constant contraction after 9 cycles, it did not completely return to its initial state. The flap displacement at the end of each actuation cycle, or 'residual' displacement ($\overline{u}_{f,res}$), is plotted at a magnified scale in Figure 4.11B, showing an evolving residual displacement with cycling that grew to almost 30% by the end of the experiment. The cause of this ratcheting behavior was due to incomplete temperature recovery, as shown and verified in [43] by temperature measurements.

The thrust performance was measured by the load cell, as shown in the force (P_z) history

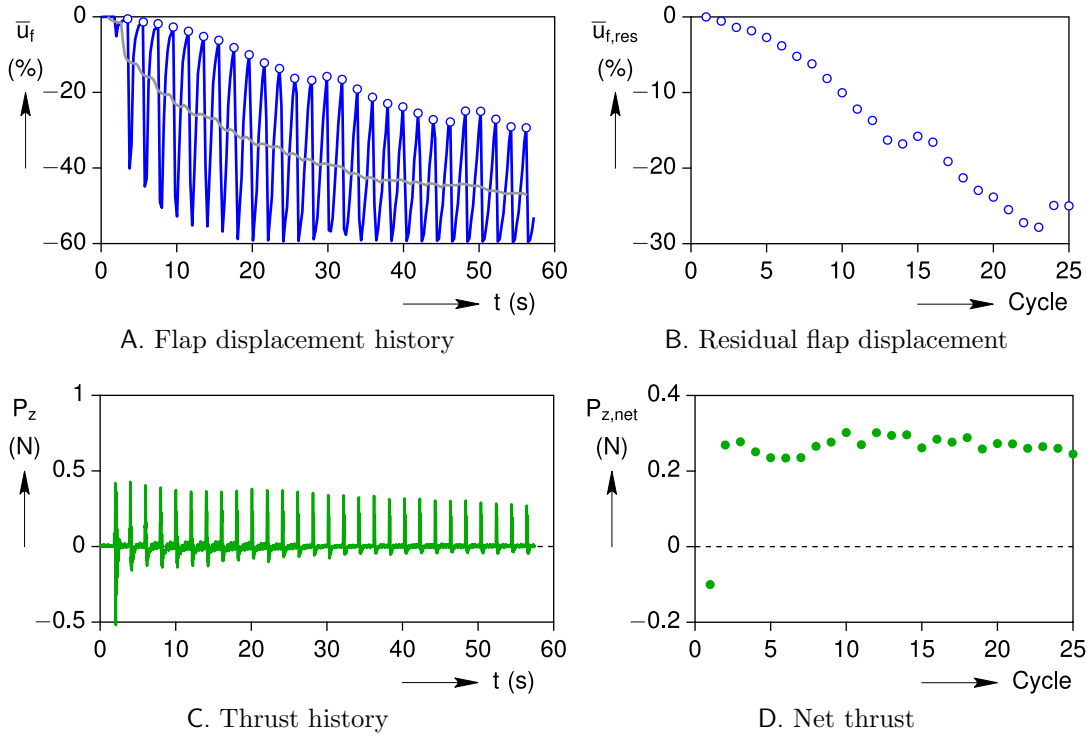

A. Flap displacement history

B. Residual flap displacement

C. Thrust history

D. Net thrust

Figure 4.11: Experimental results with 2 s actuation period at input energy of 15 J (10% duty cycle).

of Figure 4.11C. The peak thrust started near $P_{z,\max} = 0.4$ N during early cycles and decayed gradually to about 0.3 N by the end of the experiment. Likewise, negative thrust values ($P_{z,\min} < 0$) were also measured during each cycle which became smaller in magnitude after the first few cycles. We defined a net thrust as the simple sum $P_{z,\text{net}} = P_{z,\max} + P_{z,\min}$, which is plotted in Figure 4.11D. With sustained cycling, the net thrust quickly rose to a steady-state value of about $P_{z,\text{net}} = 0.25$ N.

4.4.3 Operation and design study

Numerous additional experiments were performed to evaluate the sensitivity of various design and operation parameters on thrust performance. The influence of two operation and two design parameters are presented in Figure 4.12. In all cases presented here, the period of actuation was fixed at 2 s.

In the first parameter sweep (Figures 4.12A and 4.12B), the influence of input energy was investigated on the thrust performance of the prototype robot. The duty cycle was fixed at 10% (electric current was provided for 0.2 s in each cycle), while nine experiments were performed at different input energies to the SMA spring, from 3 J to 18 J (0.2 s at 15 W to 90 W). The evolution of the net thrust at each energy level was measured during 28

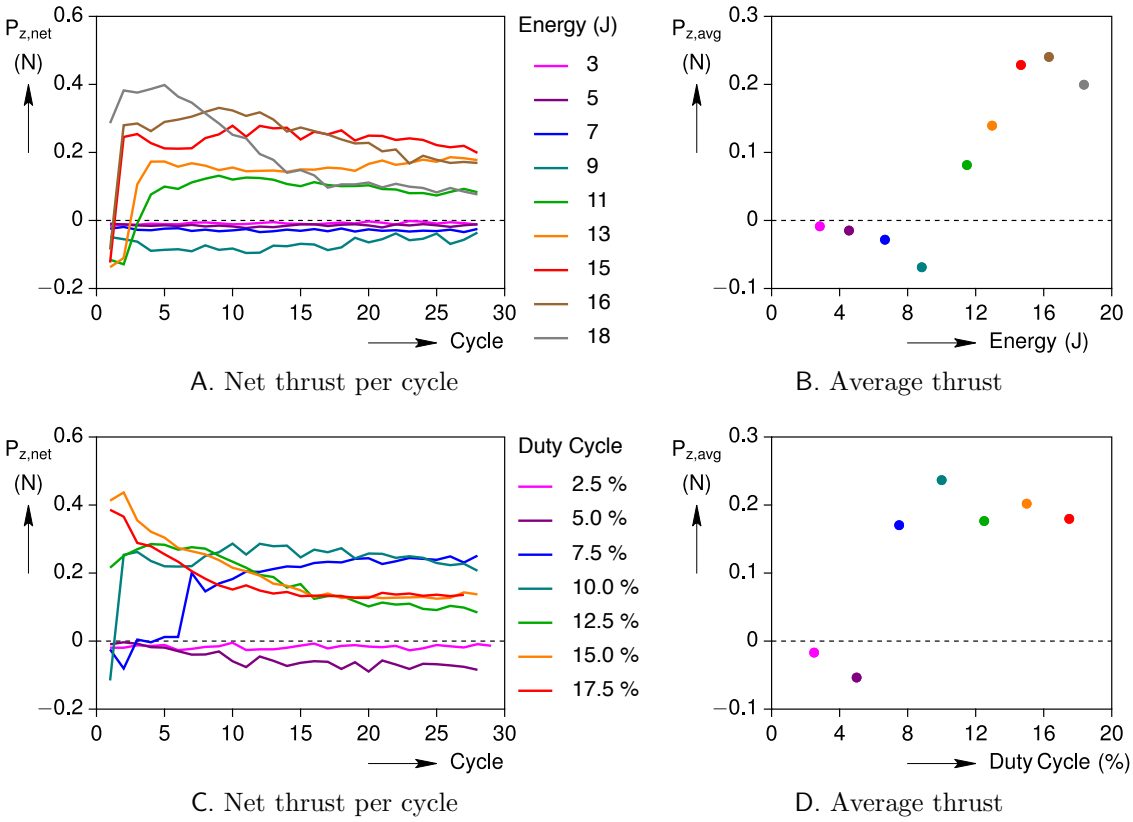

Figure 4.12: The operational parameters, input energy and duty-cycle, require threshold values to produce positive net thrust, and the thrust trends are non-monotonic with increasing values. The effects of input energy (a, b) are shown at a fixed 10% duty-cycle and 0.5 Hz actuation frequency. The effects of duty-cycle (c, d) are shown at a fixed input power of 73 W and 0.5 Hz actuation frequency.

actuation cycles (Figure 4.12A). The net thrust remained negative at the four lowest energy levels (up to 9 J). A net positive thrust first appeared at 11 J after three actuation cycles, and it reached a sustained value of about 0.1 N thereafter. The performance improved at 13 J with a sustained net thrust of almost 0.2 N during late cycles. At 15 J and 16 J the thrust was higher yet during early cycles, but it began to diminish during late cycles. At the highest energy level of 18 J, the initial thrust was about 0.4 N, but it quickly decayed with cycling and even underperformed the 13 J case by cycle 16. As shown in [43], the decrease in the propulsion performance during late cycles at high energy inputs was caused by the SMA spring becoming progressively hotter with cycling, such that it was unable to cool and relax sufficiently before the next actuation cycle. This contributed to incomplete deformation recovery. At the highest energy level, the deformation eventually reached a nearly static value with almost no oscillations (tetanic-like contraction).

To summarize the trends, the net thrust was averaged over the 28 cycles at each input

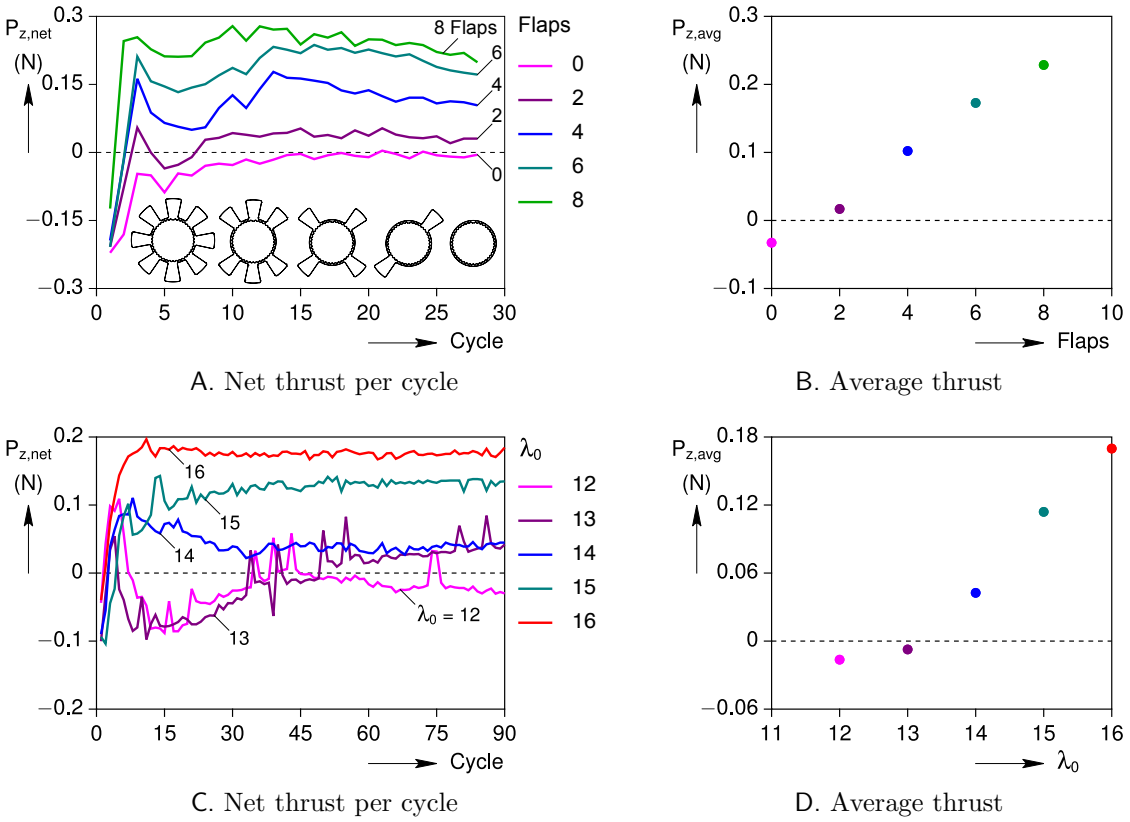

Figure 4.13: The design parameters, number of flaps and pre-stretch ratio (λ_0) of the SMA spring, require threshold values to produce positive net thrust, and the thrust trends are monotonic with increasing values. The effects of flaps (a, b) are shown at 15 J input energy, 0.5 Hz actuation frequency, and 10% duty-cycle. The effects of spring pre-stretch ratio (c, d) are shown at 3.44 J/kg input energy density, 0.5 Hz actuation frequency, and 7.5% duty-cycle.

energy level and plotted in Figure 4.12B. Interestingly, the performance only got worse (more negative) as the energy was increased at the four lowest input energies. The plot clearly shows that a threshold energy was required to achieve a positive net thrust (somewhere between 9 J and 11 J). The average thrust improved with larger intermediate energy levels (11 to 16 J), but then dropped off at excessively high input energy (18 J). While the best average thrust in this series of experiments was obtained at 16 J, it should be recognized that this was only true for the duration chosen for these experiments (28 cycles). A lower energy level would be optimal for longer experiments that involve more actuation cycles, since the thrust histories at 15 J and 16 J were decaying by the end of their experiments. Alternatively, the jellyfish robot could be given a brief rest, allowing the SMA spring to cool and recover, and then the performance shown could be repeated for another 28 cycles.

In a second parameter sweep, the influence of the duty cycle was investigated (Figures 4.12C and 4.12D). Here, the input power was held fixed at 73 W, and seven experi-

ments were performed at duty cycles between 2.5% and 17.5%. Similar to the previous energy sweep, a non-monotonic trend in the thrust performance was observed with increasing duty cycle. No net thrust (Figure 4.12C) was obtained at the two smallest duty cycles (2.5% and 5%). At the three largest duty cycles (12.5, 15, and 17.5%), the initial flap displacements (not shown here) and net thrusts were relatively large, but these decreased in later cycles. Again, this was due to excessive heating and the inability to cool and reset, thereby resulting in large residual displacements (see [43] for more details). Both cases at 15% and 17.5% duty cycle, resulted in a tetanic-like contractions by the experiments' end. Better performance was achieved at intermediate duty cycles, 7.5 and 10%, and they demonstrated a tradeoff between them. The case with 10% duty cycle reached a larger net thrust in fewer cycles than the 7.5% duty cycle case, but this came at the expense of a larger residual displacement near the end of the experiment. Thus, the 10% duty cycle would be the optimal choice (average thrust of 0.25 N) for the jellyfish robot to sprint quickly, but the 7.5% duty cycle would be the better choice (average thrust of 0.18 N) for long distance swimming.

A new study was performed on two design parameters. The number of flaps was the first design parameter varied, where for each successive experiment the same jellyfish robot was modified by removing two flaps at a time to maintain symmetry of the robot (Figures 4.13A and 4.13B). The input energy was 15 J and the duty cycle was 10%, and five experiments (28 actuation cycles each) were performed on robots with 0, 2, 4, 6, and 8 flaps. As shown in Figure 4.13A the net thrust/cycle remained negative during all cycles for the robot with no flaps. A net positive thrust first appeared for the two flap robot after eight actuation cycles, but its subsequent value remained quite small. With four flaps the thrust remained positive after early cycles and, for six flaps and eight flaps, the performance improved further. The trend was monotonic with increasing flap number, shown more clearly by averaging the net thrust over all 28 cycles for each case (Figure 4.13B). Thus, more flaps produced better performance, yet it is not clear if more than eight flaps (each narrower) would give further improvement. Finally, the influence of the second design parameter, the pre-stretch ratio of the SMA spring (λ_0), was investigated (Figures 4.13C and 4.13D) for robots with all eight flaps and a duty cycle of 7.5%. In this study, a different robot was fabricated for each experiment. The final spring length was fixed by the circumference of the robot's central disk, so the initial SMA spring length had to be decreased (fewer coils) as the pre-stretch was increased. A fixed input voltage would, therefore, produce a different temperature change due to the different mass of the SMA springs, which would obscure the effects of the pre-stretch alone. Consequently, the input energy density was held nearly constant at 3.44 J/kg, and five experiments were performed for 90 actuation cycles at pre-stretch ratios of $\lambda_0 = 12$, 13, 14, 15, and 16. The corresponding energy inputs per cycle were 13.9 J, 12.8 J, 11.9 J,

11.1 J, and 10.4 J.

It can be seen that at $\lambda_0 = 12$ (Figure 4.13C), the robot was unable to maintain a positive net thrust. Although not shown here, this was a result of a significant amount of unrecovered deformation at the end of each cycle. For a spring pre-stretch ratio of $\lambda_0 = 13$, the robot experienced a significant drop in the net thrust after the fifth cycle. The performance gradually improved, however, after 50 cycles to generate a small positive net thrust of about 0.03 N by the end of 90 cycles. Nevertheless, the average thrust over all cycles was still slightly negative (Figure 4.13D). For $\lambda_0 = 14$, the robot sustained a net positive thrust, but its performance deteriorated after an initial peak near 0.1 N to an almost steady value of 0.04 N after 40 cycles. At $\lambda_0 = 15$, the net positive thrust generally grew and reached an asymptote near 0.13 N after about 40 cycles, which is more than a three-fold increase in steady-state thrust compared to the previous pre-stretch ratio. This improvement was attributed mostly to the faster cooling of the SMA spring as the distance between adjacent coils (the pitch) was larger at higher stretch ratios. The thrust performance improved further for $\lambda_0 = 16$, where the net positive thrust reached a steady-state value of 0.17 N after only 10 cycles. The averaged net thrusts in Figure 4.13D clearly show a monotonic increase in the thrust performance, at least for the range of the pre-stretch ratios considered here.

Note that for the operational and design study on the number of flaps, the same previously cycled SMA spring was used in all the experiments. The design study on the pre-stretch ratio, however, started with a new (uncycled) spring at the smallest stretch ratio, and the same spring was trimmed to size and reused at each successively larger pre-stretch ratio.

4.5 Conclusion

We presented a simple, compact, and high-performance biomimetic robot jellyfish that mimics the morphology and kinematics of the actual creature. The main contributions of the current study are the simplicity of design and the exploration of an alternative SMA actuation approach as the artificial contractile muscle. The design consists only of a soft rubber matrix with a single embedded SMA spring loop, which when Joule heated, achieves large deformations without the need for extra mechanical parts and joints. The buckling instability of the main body is harnessed to create an effective rowing mechanism of flaps to propel the robot under water.

A numerical finite-element simulation captures the post-buckling deformation of the robot and provides details of the deformation fields within it. This provides a useful stepping stone towards the development of design and simulation tools for the fully coupled electro-thermo-mechanical problem, which will be pursued in the future. Such modeling tools are essential

to develop a design methodology for similar underwater robots to achieve a desired level of performance.

Our experimental results demonstrates actuation cycles at similar rates to previous attempts at biomimetic underwater robots. The robot swims from the bottom to the top of a water tank in a few actuation cycles via a pulsatile motion reminiscent of an actual jellyfish. It achieves swimming strokes of near 40 mm per cycle and a net steady-state propulsive thrust of 0.25 N when operated at 0.5 Hz frequency. An experimental parameter study reveals the influence of the input energy, duty cycle, number of flaps, and pre-stretch of the spring on the thrust performance of the robot. The performance is non-monotonic with the input energy and duty cycle, indicating the existence of a sweet spot that might be exploited in the robot's operation. It also reveals tradeoffs, depending on whether speed or endurance is preferred. In the range of parameters studied, the performance shows monotonic improvement with the number of flaps and pre-stretch of the SMA spring.

CHAPTER 5

Conclusions and Future Work

5.1 Conclusions

Inspired by the shape shifting capabilities of biological systems, this work has contributed the following advancements to the fields of cardiac muscle cells MCT, shape morphing inflatables, and soft robotics.

1. As a computational tool to interpret the ongoing *in vitro* Cell-in-Gel experiments, we developed a 3-D mechanical analysis of an isolated cardiomyocyte contracting in various hydrogels. The mathematical model was based on the viscoelastic generalization of the elastic Eshelby inclusion solution, which provided realistic predictions of the time-dependent mechanical fields in the Cell-in-Gel system.

2. The model was used to quantify the cell's mechanical stress and to explore the cell's response to different levels of afterload.

3. Consistent with experimental data, the model also identified a closed-loop MCT control that autoregulated cell's contraction, thereby added a new feedback feature to the current paradigm of feed-forward cardiac excitation-Ca^{2+}signaling-contraction coupling.

4. While the heart's adaptive response to load changes is usually attributed to neurohormonal (autonomic) regulation, our study showed that intrinsic autoregulation within a single cardiomyocyte also plays a major role.

5. We investigated the inflation of shape morphing synthetic soft composites with architectured properties and explored several feasible 3-D shapes that can be achieved through the inflation of an initially flat rubber membrane with nonuniform geometrical and material properties.

6. Several axisymmetric and nonaxisymmetric morphed geometries were studied and photogrammetry was employed to track the deformation profiles and change in mechanical fields during the inflation process.

7. We performed an FEA parametric study regarding the influence of geometrical nonuniformities on the response and instabilities of axisymmetric membranes.

8. In order to have confidence in the numerical findings, we validated the adopted hyperelastic energy density model for the FEA, against the experimentally measured data and showed very good agreements in a wide range of the response.

9. We demonstrated that by tailoring the distribution of materials properties in the membrane, more complicated motions including negative Gaussian curvatures and twist can be achieved during inflation.

10. Our rubber-based prototypes provided a convenient basis for conceptual scientific and design explorations in shape morphing inflatable structures.

11. Motivated by the swimming mechanisms of jellyfish, we developed a novel concept for a shape morphing soft biomimetic underwater robot that imitates the shape and kinematics of a typical jellyfish. A loop of SMA spring, serving as the artificial muscle, embedded in a soft silicone rubber, as the body of the robot, was explored for the first time in the context of underwater robotics.

12. Compared to previous attempts by other researchers to design and fabricate a synthetic jellyfish, our prototype achieved comparable performance in a simpler, compact, and solid-state design.

13. We successfully harnessed the buckling instability of the robot's main body to generate thrust and achieved a hybrid jetting and rowing locomotion mechanism.

5.2 Future work

The recommendations for future work on soft shape morphing systems include extensions of the current research and explorations of new ideas in this field. A short list of suggestions and ideas for future studies is provided below.

In cardiomyocyte contraction autoregulation:

1. To use the actual 3D geometry of different cells and perform viscoelastic FEA on the actual geometries and compare the results with the predictions of our viscoelastic

ellipsoidal inclusion assumption in terms of the minimum, average, maximum values of the field quantities.

2. Adding the affect of pre-load on the cell to measure the fast autoregulatory response of the myocyte in the framework of Frank-Starling mechanism.

3. Developing an approach for real-time measurement of the stress field during the *in vitro* experiments, potentially in the form of stress-sensitive dyes.

In architectured membranes:

1. To explore more patterns of nonuniformity, for example auxetic patterns, to extend the applications of inflatables by achieving a wider range of motions with potential use in soft robotics.

2. To embed compliant active materials such as SMA springs and micro fiber composites in the rubber membrane to achieve more complicated motions through hybrid pressurization and thermo- or electro-mechanical actuation.

3. Extend the current study to numerically and experimentally explore the effect of pattern, stiffness, size, aspect ratio, and number of the reinforcements on the maximum twist angle of the spirally reinforced membrane.

4. To implement nonlinear constrained optimization and inverse nonlinear elasticity techniques to find the corresponding anisotropic material and thickness distribution through which an elastomeric membrane would map to the desired target 3D shape after pressurization to a certain level. To implement the proposed idea experimentally, multi-material 3D printing and multi-stage casting techniques are required to layout the computationally achieved pattern of the material and thickness distribution.

In soft robotics:

1. To add a few more SMA springs or use other compliant solid-state actuators, potentially in the flaps of the current robot jellyfish prototype, to enable underwater steering and direction change.

2. To improve the cooling capability of the current robot jellyfish design to avoid overheating of the body after several actuation cycles, potentially by adding thermally conductive fillers to the silicone body of the robot or be exposing part of the SMA spring outside the body.

3. To use feedback of temperature to autonomously adjust the input power and actuation duty-cycle in real-time to improve the swimming performance.

4. To extend the idea of silicone body with embedded SMA springs to explore other swimming mechanisms, like the undulatory motion in Anguilliform and oscillatory motion in Thunniform.

BIBLIOGRAPHY

[1] Qi J, Wu B, Feng S, Lü S, Guan C, Zhang X, Qiu D, Hu Y, Zhou Y, Li C, et al. (2017) Mechanical regulation of organ asymmetry in leaves. Nature plants 3(9):724–733

[2] Huang C, Wang Z, Quinn D, Suresh S, Hsia KJ (2018) Differential growth and shape formation in plant organs. Proceedings of the National Academy of Sciences 115(49):12359–12364

[3] Whitewoods CD, Gonçalves B, Cheng J, Cui M, Kennaway R, Lee K, Bushell C, Yu M, Piao C, Coen E (2020) Evolution of carnivorous traps from planar leaves through simple shifts in gene expression. Science 367(6473):91–96

[4] Hill BS, Findlay GP (1981) The power of movement in plants: the role of osmotic machines. Quarterly reviews of biophysics 14(2):173–222

[5] Markin VS, Volkov AG, Jovanov E (2008) Active movements in plants: mechanism of trap closure by Dionaea muscipula Ellis. Plant signaling & behavior 3(10):778–783

[6] Kempaiah R, Nie Z (2014) From nature to synthetic systems: shape transformation in soft materials. Journal of Materials Chemistry B 2(17):2357–2368

[7] Forterre Y, Skotheim JM, Dumais J, Mahadevan L (2005) How the Venus flytrap snaps. Nature 433(7024):421–425

[8] Volkov AG, Foster JC, Ashby TA, Walker RK, Johnson JA, Markin VS (2010) Mimosa pudica: electrical and mechanical stimulation of plant movements. Plant, cell & environment 33(2):163–173

[9] Guayasamin JM, Krynak T, Krynak K, Culebras J, Hutter CR (2015) Phenotypic plasticity raises questions for taxonomically important traits: a remarkable new Andean rainfrog (Pristimantis) with the ability to change skin texture. Zoological Journal of the Linnean Society 173(4):913–928

[10] Harvey C, Baliga V, Lavoie P, Altshuler D (2019) Wing morphing allows gulls to modulate static pitch stability during gliding. Journal of the Royal Society Interface 16(150):20180641

[11] Valasek J (2012) Morphing aerospace vehicles and structures, vol. 57. John Wiley & Sons

[12] Guerrero JE, Maestro D, Bottaro A (2012) Biomimetic spiroid winglets for lift and drag control. Comptes Rendus Mecanique 340(1-2):67–80

[13] https://bioactive-collagen-peptides.com/effects-muscles, accessed. November 20, 2020.

[14] Sandow A (1952) Excitation-contraction coupling in muscular response. The Yale journal of biology and medicine 25(3):176

[15] http://cnx.org/content/m44788/latest/Figure_38_04_06f.png, creative Commons Attribution 3.0 Unported (CC BY 3.0) from OpenStax College, Muscle Contraction and Locomotion. October 17, 2013.

[16] Bers DM (2002) Cardiac excitation–contraction coupling. Nature 415(6868):198–205

[17] Oliver K, Seddon A, Trask RS (2016) Morphing in nature and beyond: a review of natural and synthetic shape-changing materials and mechanisms. Journal of Materials Science 51(24):10663–10689

[18] WAINWRIGHT PC, Kraklau DM, BENNETT AF (1991) Kinematics of tongue projection in Chamaeleo oustaleti. Journal of experimental biology 159(1):109–133

[19] Allen JJ, Bell GR, Kuzirian AM, Hanlon RT (2013) Cuttlefish skin papilla morphology suggests a muscular hydrostatic function for rapid changeability. Journal of morphology 274(6):645–656

[20] Vogel S (2013) Comparative biomechanics: life's physical world. Princeton University Press

[21] https://www.nasa.gov/ames, credits: NASA/Kenneth Cheung. Accessed. November 20, 2020.

[22] Tomatsu I, Peng K, Kros A (2011) Photoresponsive hydrogels for biomedical applications. Advanced drug delivery reviews 63(14-15):1257–1266

[23] Barbarino S, Bilgen O, Ajaj RM, Friswell MI, Inman DJ (2011) A review of morphing aircraft. Journal of intelligent material systems and structures 22(9):823–877

[24] Jenett B, Calisch S, Cellucci D, Cramer N, Gershenfeld N, Swei S, Cheung KC (2017) Digital morphing wing: active wing shaping concept using composite lattice-based cellular structures. Soft robotics 4(1):33–48

[25] Hartl D, Volk B, Lagoudas DC, Calkins F, Mabe J (2006) Thermomechanical characterization and modeling of Ni60Ti40 SMA for actuated chevrons. In ASME International Mechanical Engineering Congress and Exposition, vol. 47659, 281–290

[26] Mabe J, Calkins F, Butler G (2006) Boeing's variable geometry chevron, morphing aerostructure for jet noise reduction. In 47th AIAA/ASME/ASCE/AHS/ASC Structures, Structural Dynamics, and Materials Conference 14th AIAA/ASME/AHS Adaptive Structures Conference 7th, 2142

[27] Stuart MAC, Huck WT, Genzer J, Müller M, Ober C, Stamm M, Sukhorukov GB, Szleifer I, Tsukruk VV, Urban M, et al. (2010) Emerging applications of stimuli-responsive polymer materials. Nature materials 9(2):101–113

[28] Zhuang J, Gordon MR, Ventura J, Li L, Thayumanavan S (2013) Multi-stimuli responsive macromolecules and their assemblies. Chemical Society Reviews 42(17):7421–7435

[29] Kushner AM, Guan Z (2011) Modular design in natural and biomimetic soft materials. Angewandte Chemie International Edition 50(39):9026–9057

[30] Hu Z, Zhang X, Li Y (1995) Synthesis and application of modulated polymer gels. Science 269(5223):525–527

[31] Naficy S, Gately R, Gorkin III R, Xin H, Spinks GM (2017) 4D printing of reversible shape morphing hydrogel structures. Macromolecular Materials and Engineering 302(1):1600212

[32] Rizou A, Soriano E, Sastre R (2019) PNEULASTICS, pneumatically activated differentiated stretchable membranes. In Proceedings of IASS Annual Symposia, vol. 2019, 1–9, International Association for Shell and Spatial Structures (IASS)

[33] Klein Y, Efrati E, Sharon E (2007) Shaping of elastic sheets by prescription of non-Euclidean metrics. Science 315(5815):1116–1120

[34] Wu ZL, Moshe M, Greener J, Therien-Aubin H, Nie Z, Sharon E, Kumacheva E (2013) Three-dimensional shape transformations of hydrogel sheets induced by small-scale modulation of internal stresses. Nature communications 4(1):1–7

[35] Boley JW, van Rees WM, Lissandrello C, Horenstein MN, Truby RL, Kotikian A, Lewis JA, Mahadevan L (2019) Shape-shifting structured lattices via multimaterial 4D printing. Proceedings of the National Academy of Sciences 116(42):20856–20862

[36] Ford MJ, Ambulo CP, Kent TA, Markvicka EJ, Pan C, Malen J, Ware TH, Majidi C (2019) A multifunctional shape-morphing elastomer with liquid metal inclusions. Proceedings of the National Academy of Sciences 116(43):21438–21444

[37] Siéfert E, Reyssat E, Bico J, Roman B (2019) Bio-inspired pneumatic shape-morphing elastomers. Nature materials 18(1):24–28

[38] Fernandes R, Gracias DH (2012) Self-folding polymeric containers for encapsulation and delivery of drugs. Advanced drug delivery reviews 64(14):1579–1589

[39] Vunjak-Novakovic G, Scadden DT (2011) Biomimetic platforms for human stem cell research. Cell stem cell 8(3):252–261

[40] Maeda S, Hara Y, Sakai T, Yoshida R, Hashimoto S (2007) Self-walking gel. Advanced Materials 19(21):3480–3484

[41] Shepherd RF, Ilievski F, Choi W, Morin SA, Stokes AA, Mazzeo AD, Chen X, Wang M, Whitesides GM (2011) Multigait soft robot. Proceedings of the national academy of sciences 108(51):20400–20403

[42] Kazemi-Lari MA, Shaw JA, Wineman AS, Shimkunas R, Izu LT, Chen-Izu Y (2018) Viscoelastic Eshelby Analysis of Cardiomyocyte Contraction in the Cell-In-Gel System. In Conference on Smart Materials, Adaptive Structures and Intelligent Systems (SMASIS 2018), vol. 2: Mechanics and Behavior of Active Materials; Integrated System Design and Implementation; Bioinspired Smart Materials and Systems; Energy Harvesting, ASME, San Antonio, TX

[43] Kazemi-Lari MA, Dostine AD, Zhang J, Wineman AS, Shaw JA (2019) Robotic jellyfish actuated with a shape memory alloy spring. In AL Raul J Martin-Palma Mato Knez, editor, Proceedings of SPIE, vol. 10965: Bioinspiration, Biomimetics, and Bioreplication IX, 1096504–1 to 1096504–17, SPIE, Denver, CO

[44] Paley DA, Wereley NM, Bioinspired Sensing, Actuation, and Control in Underwater Soft Robotic Systems

[45] Von Anrep G (1912) On the part played by the suprarenals in the normal vascular reactions of the body. The Journal of physiology 45(5):307–317

[46] Patterson S, Piper H, Starling E (1914) The regulation of the heart beat. The Journal of physiology 48(6):465–513

[47] Starling EH (1918) The Linacre lecture on the law of the heart. Longmans, Green, & Company

[48] Moss RL, Fitzsimons DP (2002), Frank-Starling relationship: long on importance, short on mechanism

[49] de Tombe PP, Mateja RD, Tachampa K, Mou YA, Farman GP, Irving TC (2010) Myofilament length dependent activation. Journal of molecular and cellular cardiology 48(5):851–858

[50] Bollensdorff C, Lookin O, Kohl P (2011) Assessment of contractility in intact ventricular cardiomyocytes using the dimensionless 'Frank–Starling Gain' index. Pflügers Archiv-European Journal of Physiology 462(1):39–48

[51] Cingolani HE, Pérez NG, Cingolani OH, Ennis IL (2012) The Anrep effect: 100 years later. American Journal of Physiology-Heart and Circulatory Physiology 304(2):H175–H182

[52] Chen-Izu Y, Izu LT (2017) Mechano-chemo-transduction in cardiac myocytes. The Journal of physiology 595(12):3949–3958

[53] Schönleitner P, Schotten U, Antoons G (2017) Mechanosensitivity of microdomain calcium signaling in the heart. Progress in biophysics and molecular biology 130:288–301

[54] Izu LT, Kohl P, Boyden PA, Miura M, Banyasz T, Chiamvimonvat N, Trayanova N, Bers DM, Chen-Izu Y (2019) Mechano-electric and mechano-chemo-transduction in cardiomyocytes. The Journal of Physiology

[55] Jian Z, Han H, Zhang T, Puglisi J, Izu LT, Shaw JA, Onofiok E, Erickson JR, Chen YJ, Horvath B, Shimkunas R, Pan T, Chan J, Banyasz T, Chiamvimonvat N, Bers DM, Lam KS, Chen-Izu Y (2014) Mechanochemotransduction During Cardiac Contraction Is Mediated by Localized Nitric Oxide Signaling. Science Signaling 7(317):1–9

[56] Eshelby JD (1957) The determination of the elastic field of an ellipsoidal inclusion, and related problems. Proc Royal Soc A 241(1226):376–396

[57] Eshelby JD (1959) The Elastic Field Outside an Ellipsoidal Inclusion. Proc Roy Soc London Series A, Math & Phys Sci 252(1271):561–569

[58] Shaw JA, Izu LT, Chen-Izu Y (2013) Mechanical Analysis of Single Myocyte Contraction in a 3-D Elastic Matrix. PLOS ONE 8(10):e75492

[59] Hashin Z (1965) Viscoelastic Behavior of Heterogeneous Media. Journal of Applied Mechanics 32(3):630–636

[60] Hegyi B, Bányász T, Izu LT, Belardinelli L, Bers DM, Chen-Izu Y (2018) β-adrenergic regulation of late Na^+ current during cardiac action potential is mediated by both PKA and CaMKII. Journal of molecular and cellular cardiology 123:168–179

[61] Wineman AS, Rajagopal KR (2000) Mechanical Response of Polymers. Cambridge University Press

[62] Prosser BL, Khairallah RJ, Ziman AP, Ward CW, Lederer WJ (2013) X-ROS signaling in the heart and skeletal muscle: Stretch-dependent local ROS regulates $[Ca^{2+}]_i$. Journal of Molecular and Cellular Cardiology 58:172

[63] Barthélémy JF, Giraud A, Lavergne F, Sanahuja J (2016) The Eshelby inclusion problem in ageing linear viscoelasticity. International Journal of Solids and Structures 97:530–542

[64] Wolfram Research, Inc Mathematica, Version 12.0. Champaign, IL, 2019

[65] Kirk MM, Izu LT, Chen-Izu Y, McCulle SL, Wier WG, Balke CW, Shorofsky SR (2003) Role of the transverse-axial tubule system in generating calcium sparks and calcium transients in rat atrial myocytes. The Journal of physiology 547(2):441–451

[66] Chen-Izu Y, McCulle SL, Ward CW, Soeller C, Allen BM, Rabang C, Cannell MB, Balke CW, Izu LT (2006) Three-dimensional distribution of ryanodine receptor clusters in cardiac myocytes. Biophysical journal 91(1):1–13

[67] Jacot JG, Kita-Matsuo H, Wei KA, Chen HV, Omens JH, Mercola M, McCulloch AD (2010) Cardiac myocyte force development during differentiation and maturation. Annals of the New York Academy of Sciences 1188:121

[68] Granzier HL, Irving TC (1995) Passive tension in cardiac muscle: contribution of collagen, titin, microtubules, and intermediate filaments. Biophysical journal 68(3):1027–1044

[69] Zile MR, Baicu CF, Gaasch WH (2004) Diastolic heart failure—abnormalities in active relaxation and passive stiffness of the left ventricle. New England Journal of Medicine 350(19):1953–1959

[70] Granzier HL, Labeit S (2004) The giant protein titin: a major player in myocardial mechanics, signaling, and disease. Circulation research 94(3):284–295

[71] Anastasi G, Cutroneo G, Gaeta R, Di Mauro D, Arco A, Consolo A, Santoro G, Trimarchi F, Favaloro A (2009) Dystrophin-glycoprotein complex and vinculin-talin-integrin system in human adult cardiac muscle. International journal of molecular medicine 23(2):149–159

[72] Reed UC (2009) Congenital muscular dystrophy. Part I: a review of phenotypical and diagnostic aspects. Arquivos de neuro-psiquiatria 67(1):144–168

[73] Reed UC (2009) Congenital muscular dystrophy. Part II: a review of pathogenesis and therapeutic perspectives. Arquivos de neuro-psiquiatria 67(2A):343–362

[74] Cathey HM, Pierce DL (2007) Development of the NASA ultra-long duration balloon. In NASA Science Technology Conference, 19–21

[75] Freeland R, Veal G (1998) Significance of the inflatable antenna experiment technology. In 39th AIAA/ASME/ASCE/AHS/ASC Structures, Structural Dynamics, and Materials Conference and Exhibit, 2104

[76] Xu Y, Guan Fl (2012) Structure design and mechanical measurement of inflatable antenna. Acta Astronautica 76:13–25

[77] Babuscia A, Corbin B, Knapp M, Jensen-Clem R, Van de Loo M, Seager S (2013) Inflatable antenna for cubesats: Motivation for development and antenna design. Acta Astronautica 91:322–332

[78] Wang C, Wang Y, Lian P, Xue S, Xu Q, Shi Y, Jia Y, Du B, Liu J, Tang B (2020) Space Phased Array Antenna Developments: A Perspective on Structural Design. IEEE Aerospace and Electronic Systems Magazine 35(7):44–63

[79] Lichodziejewski D, Veal G, Helms R, Freeland R, Kruer M (2003) Inflatable rigidizable solar array for small satellites. In 44th AIAA/ASME/ASCE/AHS/ASC Structures, Structural Dynamics, and Materials Conference, 1898

[80] Litteken DA (2019) Inflatable technology: using flexible materials to make large structures. In Electroactive Polymer Actuators and Devices (EAPAD) XXI, vol. 10966, 1096603, International Society for Optics and Photonics

[81] Jones JA, Wu JJ (1999) Inflatable rovers for planetary applications. In Mobile Robots XIV, vol. 3838, 63–68, International Society for Optics and Photonics

[82] Marraffa L, Kassing D, Baglioni P, Wilde D, Walther S, Pitchkhadze K, Finchenko V (2000) Inflatable re-entry technologies: flight demonstration and future prospects. ESA bulletin 78–85

[83] Valle GD, Litteken D, Jones TC (2019) Review of Habitable Softgoods Inflatable Design, Analysis, Testing, and Potential Space Applications. In AIAA Scitech 2019 Forum, 1018

[84] Oñate E, Kröplin B (2006) Textile composites and inflatable structures, vol. 3. Springer Science & Business Media

[85] Thomas JC, Schoefs F, Caprani C, Rocher B (2020) Reliability of inflatable structures: Challenge and first results. European Journal of Environmental and Civil Engineering 24(10):1533–1557

[86] Barton B (2016) Recent Work on the Design and Construction of Air Inflated Structures. Procedia Engineering 155:47–60

[87] Green AE, Adkins JE (1960) Large elastic deformations and non-linear continuum mechanics. Clarendon Press

[88] Yang WH, Feng WW (1970) On Axisymmetrical Deformations of Nonlinear Membranes. Journal of Applied Mechanics 37(4):1002–1011, doi:10.1115/1.3408651

[89] Tielking JT, Feng WW (1974) The Application of the Minimum Potential Energy Principle to Nonlinear Axisymmetric Membrane Problems. Journal of Applied Mechanics 41(2):491–496, doi:10.1115/1.3423315

[90] Feng WW, Huang P (1974) On the Inflation of a Plane Nonlinear Membrane. Journal of Applied Mechanics 41(3):767–771, doi:10.1115/1.3423385

[91] Oden JT (1972) Finite Elements of Nonlinear Continua. McGraw-Hill

[92] Leonard JW, Verma VK (1976) Doubled-Curved Element for Mooney-Rivlin Membranes. Journal of the Engineering Mechanics Division 102(4):625–641

[93] Charrier J, Shrivastava S, Wu R (1987) Free and constrained inflation of elastic membranes in relation to thermoformingaxisymmetric problems. The Journal of Strain Analysis for Engineering Design 22(2):115–125

[94] Charrier J, Shrivastava S, Wu R (1989) Free and constrained inflation of elastic membranes in relation to thermoformingnon-axisymmetric problems. The Journal of Strain Analysis for Engineering Design 24(2):55–74

[95] PhotoModeler Technologies PhotoModeler Premium, Version 2020.2.1. Vancouver, BC, Canada, 2020

[96] Demirkoparan H, Pence TJ (2018) Swelling–twist interaction in fiber-reinforced hyperelastic materials: the example of azimuthal shear. Journal of Engineering Mathematics 109(1):63–84

[97] Griffiths G (2002) Technology and applications of autonomous underwater vehicles, vol. 2. CRC Press

[98] Nicholson J, Healey A (2008) The present state of autonomous underwater vehicle (AUV) applications and technologies. Marine Technology Society Journal 42(1):44–51

[99] Chu WS, Lee KT, Song SH, Han MW, Lee JY, Kim HS, Kim MS, Park YJ, Cho KJ, Ahn SH (2012) Review of biomimetic underwater robots using smart actuators. International journal of precision engineering and manufacturing 13(7):1281–1292

[100] Gemmell BJ, Costello JH, Colin SP, Stewart CJ, Dabiri JO, Tafti D, Priya S (2013) Passive energy recapture in jellyfish contributes to propulsive advantage over other metazoans. Proceedings of the National Academy of Sciences 110(44):17904–17909

[101] Colin SP, Costello JH (2002) Morphology, swimming performance and propulsive mode of six co-occurring hydromedusae. Journal of experimental biology 205(3):427–437

[102] McHenry MJ, Jed J (2003) The ontogenetic scaling of hydrodynamics and swimming performance in jellyfish (Aurelia aurita). Journal of Experimental Biology 206(22):4125–4137

[103] Dabiri JO, Colin SP, Costello JH, Gharib M (2005) Flow patterns generated by oblate medusan jellyfish: field measurements and laboratory analyses. Journal of Experimental Biology 208(7):1257–1265

[104] Majidi C (2014) Soft robotics: a perspective—current trends and prospects for the future. Soft Robotics 1(1):5–11

[105] Yang Y, Ye X, Guo S (2007) A new type of jellyfish-like microrobot. In Integration Technology, 2007. ICIT'07. IEEE International Conference on, 673–678, IEEE

[106] Villanueva A, Joshi K, Blottman J, Priya S (2010) A bio-inspired shape memory alloy composite (BISMAC) actuator. Smart Materials and Structures 19(2):025013

[107] Villanueva A, Smith C, Priya S (2011) A biomimetic robotic jellyfish (Robojelly) actuated by shape memory alloy composite actuators. Bioinspiration & biomimetics 6(3):036004

[108] Gao F, Wang Z, Wang Y, Wang Y, Li J (2014) A prototype of a biomimetic mantle jet propeller inspired by cuttlefish actuated by SMA wires and a theoretical model for its jet thrust. Journal of Bionic Engineering 11(3):412–422

[109] Kim HJ, Song SH, Ahn SH (2012) A turtle-like swimming robot using a smart soft composite (SSC) structure. Smart Materials and Structures 22(1):014007

[110] https://live.staticflickr.com/2850/8843118889_46fa640013_b.jpg, accessed: 2019-06-01

[111] https://dsvphotos.smugmug.com/Reference-Years/Z2013-2014-2015/i-KqQ4854/A, accessed: 2019-06-01

[112] Churchill CB, Shaw JA (2008) Shakedown Response of Conditioned Shape Memory Alloy Wire. In Behavior and Mechanics of Multifunctional and Composite Materials, Proceedings of the SPIE 15th Annual International Symposium on Smart Structures and Materials, vol. 6929, 6929F

[113] Bryan GH (1890) On the stability of a plane plate under thrusts in its own plane, with applications to the "buckling" of the sides of a ship. Proceedings of the London Mathematical Society 1(1):54–67

[114] Bulson PS (1969) The stability of flat plates. Elsevier Publishing Company

[115] Friedrichs KO, Stoker J (1941) Buckling of the circular plate beyond the critical thrust

[116] Bloom F, Coffin D (2000) Handbook of thin plate buckling and postbuckling. Chapman and Hall/CRC

[117] Alfutov NA (2013) Stability of elastic structures. Springer Science & Business Media